Master's Theses and Capstones                                    Student Scholarship

Winter 2009

# Analytical model prediction and experimental investigation of nanoforming of Bulk Metallic Glass

Catherine Mros
*University of New Hampshire, Durham*

Follow this and additional works at: https://scholars.unh.edu/thesis

ANALYTICAL MODEL PREDICTION AND EXPERIMENTAL INVESTIGATION
OF NANOFORMING OF BULK METALLIC GLASS

BY

CATHERINE MROS
BS, Clarkson University, 2006

THESIS

Submitted to the University of New Hampshire
in Partial Fulfillment of
the Requirements for the Degree of

Master of Science

in

Mechanical Engineering

December, 2009

UMI Number: 1481713

# UMI®

Dissertation Publishing
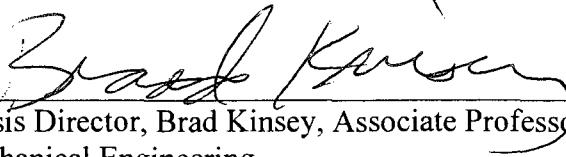
# ProQuest®

This thesis has been examined and approved.

Thesis Director, Brad Kinsey, Associate Professor in
Mechanical Engineering

Todd Gross, Professor and Chair in Mechanical
Engineering

Yannis Korkolis, Assistant Professor in Mechanical
Engineering

12/15/2009

Date

# AKNOWEGEMENTS

# TABLE OF CONTENTS

# LIST OF TABLES

# LIST OF FIGURES

ABSTRACT

NANOFORMING OF BULK METALLIC GLASS

by

Catherine Mros

University of New Hampshire, December, 2009

High aspect ratio nanostructures have been successfully fabricated in supercooled Bulk Metallic Glass (BMG) by molding against patterned Silicon. Nanoforming allows for a high rate manufacturing of nanostructures. In past research, two theoretical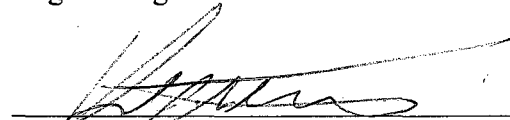 models to analyze the nanoforming process were created. These models were combined and further developments were made. This model is used to predict the depth of fill for a trench feature at a particular location on the mold based on molding parameters specified. The effects of surface tension of the BMG were also considered. An experimental setup was constructed and experiments were performed in an attempt to investigate the highest achievable aspect ratio for a specified size feature and known molding parameters to compare with the theoretical model. While flow into the trench features did not occur, observations confirmed that the pressures at the centers of molds were higher than at the edges, which agrees with the theoretical model qualitatively.

# CHAPTER I

## INTRODUCTION

With rapidly increasing advances in technology, nanotechnology is becoming vital to the developments in miniaturization. Nanotechnology is currently being used in many types of applications including cancer identification tools, mechanical and electrical devices such as memory and DNA chips, and improved performances in sporting goods, clothing, and sunscreen. With these technological advances, there is a demand for high rate nanomanufacturing processes.

Current processes at the nanoscale can be time intensive and costly. With lithography processes such as ion beam and electron beam, material can be removed or added to a substrate based upon the type of photoresist used. For example, thin film deposition, a process by which atoms are deposited onto a substrate one layer at a time [1], is precise, yet slow and costly. Another more traditional process is lithography which is used to create integrated circuits. Again this process produces high quality parts but has high costs due to the clean room space and nanofabrication equipment required. Also features are limited to 2.5 dimensions and certain materials.

Thus there is a need for mass producing precisely patterned nanoscale features at low costs and with durable materials. The nanoforming process described in this thesis is an inexpensive mass production manufacturing process that can produce Bulk Metallic Glass (BMG) components. BMG is strong, high impact resistant, amorphous material that makes it ideal for nanoforming. The BMG formed features created with the

1

nanoforming process can be used in different ways. For example, its properties make it an ideal material to be used as a mold for other processes such as injection molding. The BMG is more robust than materials currently used and will last longer, decreasing manufacturing costs. The BMG could also be used as an initial substrate for other applications such as Ion Beam Assisted Deposition providing a high rate nanomanufacturing process for these applications to decrease manufacturing costs.

There are several types of BMGs, and numerous BMGs have been used in micro and nanoforming processes. In 2001 precision microstructures were formed into a Palladium based BMG using a silicon mold via superplastic microforming [2]. It was also shown that nanoscale features could be formed using the same process. The Si molds were fabricated with traditional nanofabrication methods. The Si molds and Pd-BMG counterparts are shown in Fig. 1-1.
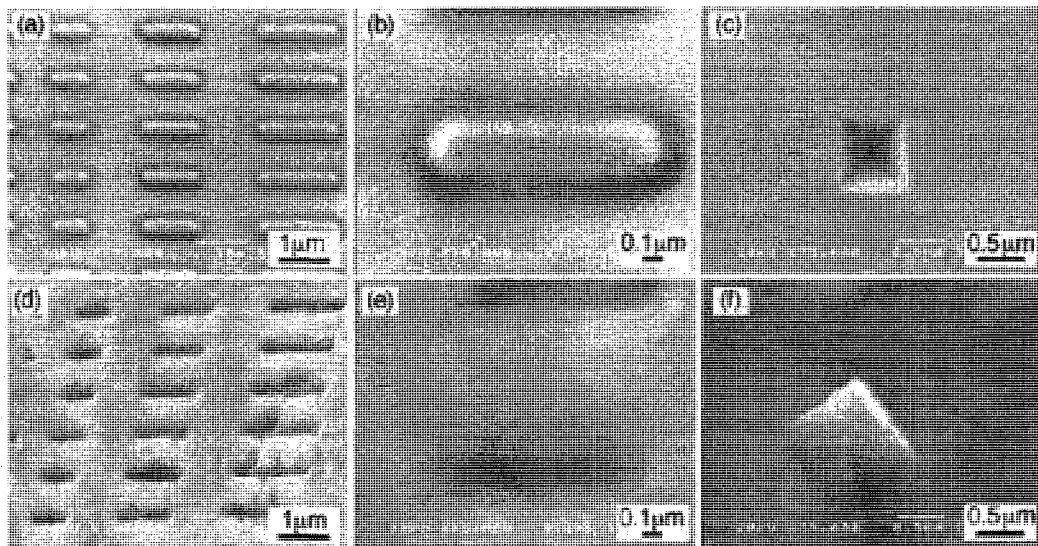


Figure 1-1: a-c) SEM images of Si fabricated dies. d-f) SEM images of Pd-BMG features formed from the Si molds. [2]

Later experiments demonstrated that other BMGs could be successfully formed into nanofeatures [3,4]. Research continued to create smaller nanoscale features. Using an embossing process, experiments were performed to find the smallest diameter rods that could be formed with the highest aspect ratio (length/diameter) [5]. SEM images of nanoformed rods in platinum based BMG are shown in Fig. 1-2. Complex, precise microparts including tweezers and gears, shown in Fig. 1-3 have been successfully fabricated using a hot embossing process [5]. The Si molds were fabricated using traditional lithography and etching techniques.
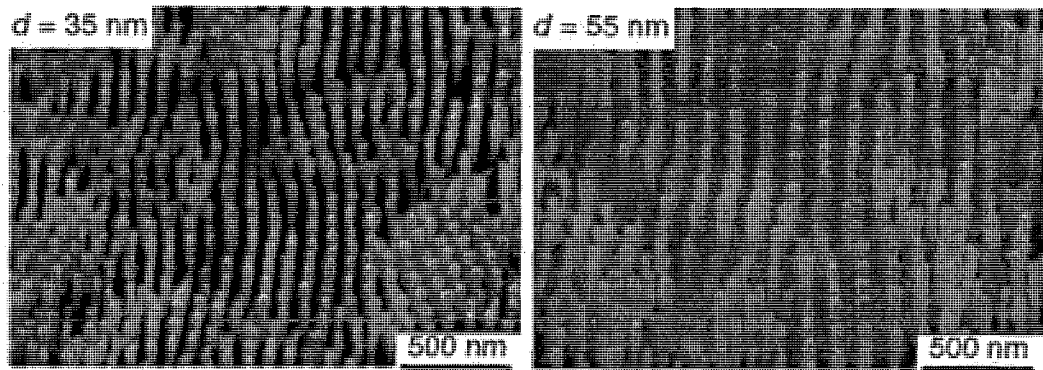


Figure 1-2: SEM images of Pt-based BMG rods by embossing. [5]
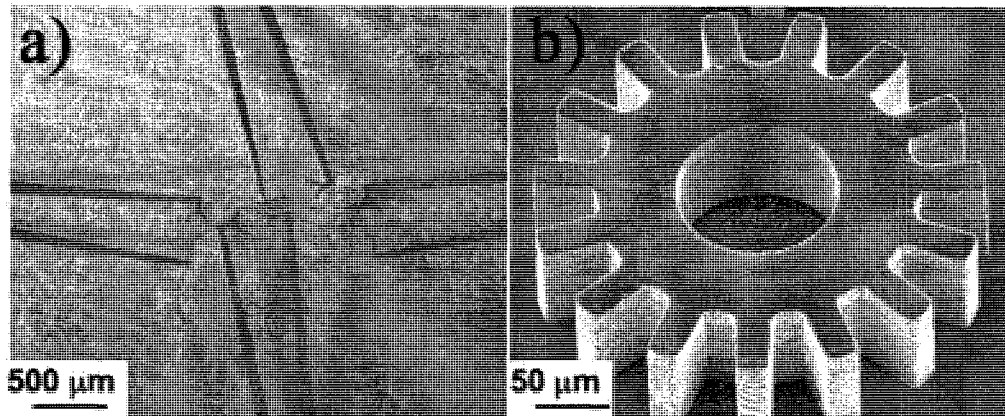


Figure 1-3: SEM images of Pt-BMG microparts: a) Microtweezers b) Microgear [5].

Geometrically complex, high aspect ratio microstructures have been successfully replicated into Zirconium based BMGs, commercially known as the Vitreloy series of alloys from LiquidMetal Technologies [6]. This has been done by molding them against patterned Silicon or $SiO_2$ substrates [4,7]. Although there are several types of BMG, the one used in this research is $Zr_{44}Be_{25}Ti_{11}Cu_{10}Ni_{10}$, or Vitreloy 1b. This particular alloy is well suited for filling high aspect ratio, complex features and withstanding high temperatures for molding processes [4].
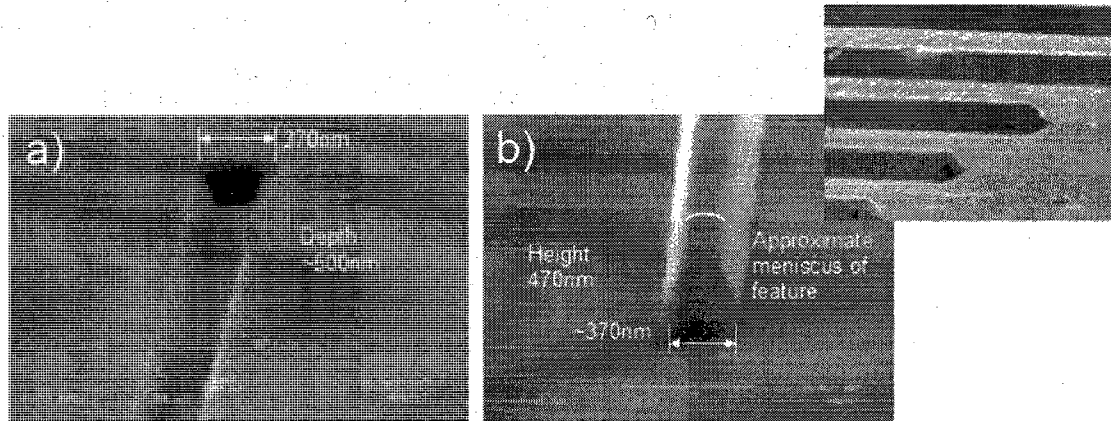


Figure 1-4: a) SEM image of Si mold. b) SEM image of Vit-1b formed features. [8,9]

The interfacial interaction between supercooled Vit-1b and the nanoscale mold material was investigated for a few mold materials. The wetability of these mold materials, which affects the BMG's ability to flow into mold features, was also examined. The results of experiments showed that the pure silicon molds were better than the $SiO_2$ for high rate nanomanufacturing processes. SEM images of the silicon mold and Zr-BMG formed features are shown in Fig. 1-4. Although pressure distribution across the mold and achievable aspect ratio were investigated, limitations of the molds led to inconclusive results [8,10,11]. In order to use the nano-thermoforming process as a high-

rate nanomanufacturing process, further understanding of the pressure distribution across a mold and the achievable aspect ratios is required.
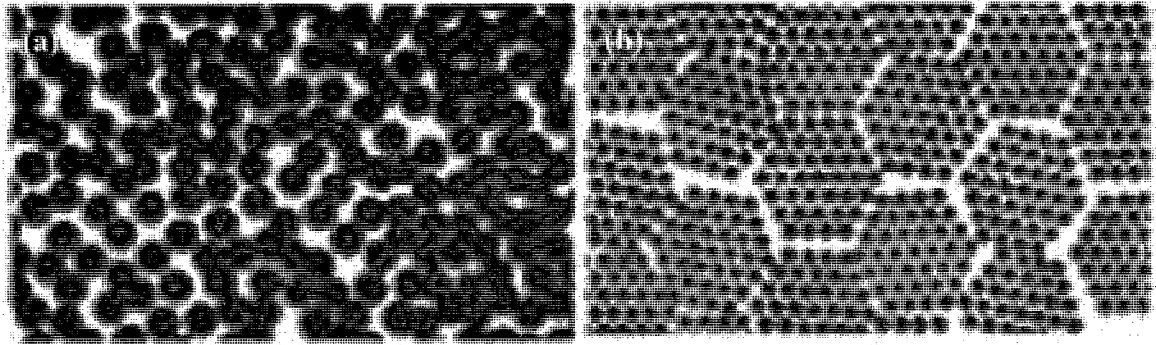


Figure 1-5: (a) Amorphous structure. (b) Polycrystalline structure. [12]

Bulk metallic glass (BMG), a typical material used in nanoforming processes has properties that are useful in forming on smaller scales. The property that allows BMG to be formed at the nanoscale is that it has an amorphous structure, i.e., it contains no metallic grains unlike typical polycrystalline metals. This causes it to be homogenous and isotropic at the atomic scale, as shown schematically in Fig. 1-5a. This is important because without a polycrystalline structure, such as the schematic of Fig. 1-5b, forming more complex shapes of smaller sizes becomes possible. Since forming is limited due to the grain boundaries, a material cannot form into a feature that is smaller than the grains of the material. This concept is illustrated in Fig. 1-6. Given, that most materials have grains too large to form on the nanoscale, a material without grains is a desirable property of a material used for nanoforming.

Grain size Dg ≈ Width of V-groove Wd

Grain size Dg << Width of V-groove Wd
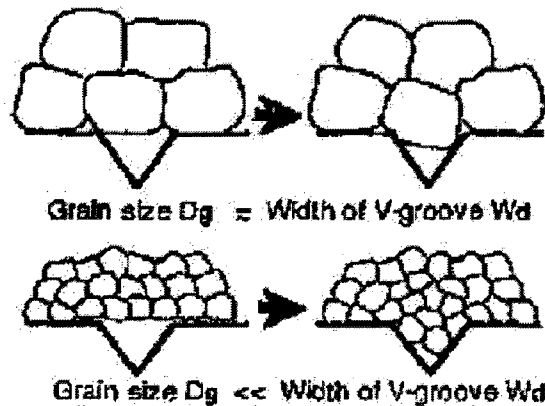
Figure 1-6: Schematic shows grain size effects forming certain size features [13].

Further understanding of this material can be obtained through a time temperature transformation (TTT) diagram as shown in Fig. 1-7. As long as the forming process stays to the left of the TTT curve the material will not crystallize. If the process causes the BMG to be heated for too long, the glass will start to form crystals and become brittle. Preventing crystallization is ideal, as the BMG remains strong with a high impact resistant.
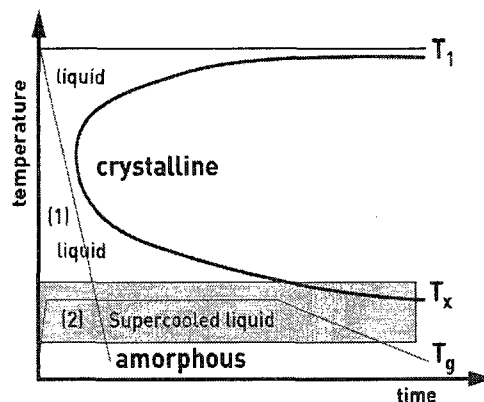


Figure 1-7: Time Temperature Transformation diagram. [14]

The molding temperature of BMG is not only important to the crystallization time, but also determines its viscosity. The viscosity controls the ability of the BMG to flow into mold features. The viscosity of Vit-1b decreases drastically as temperature is

6

increased, allowing the material to flow much easier at higher temperatures [15]. The effect of temperature on the viscosity and recrystallization time of Vit-1b is clearly shown in Fig. 1-8 [14].
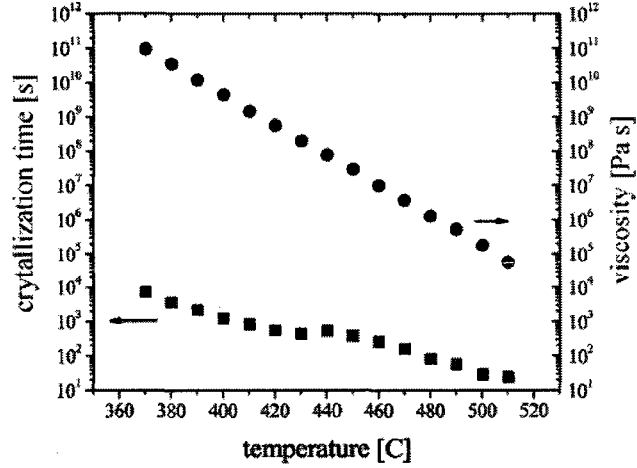


Figure 1-8: Recrystallization time and viscosity versus temperature for Vit-1b [14].

In this thesis, the nanomolding process for BMGs is further investigated by further developing a theoretical model, conducting experiments and comparing results. In Chapter II, past research conducted by Rason et al. [8] is reviewed. The surface tension of BMG is considered in Chapter III. Chapter IV develops a theoretical model for predicting the achievable depth of fill for a given time, temperature, applied pressure, and trench width. Chapter V shows the experimental setup and results. Chapter VI contains the conclusions and future work.

CHAPTER II

PAST RESEARCH

## 2.1 Thin Film Model

While a single pressure is applied to the BMG and mold chip during the nanoforming process, the pressure distribution would not be uniform since the BMG behaves as a Newtonian fluid. To quantify the pressure distribution across the BMG during the molding process, a Thin Film model was developed by Rason et al. [8]. The assumptions in the model are:

o  For a film thickness which is much smaller than the film width (i.e., a 5mm x 5mm mold with an initial BMG thickness of approximately 1mm that is rapidly decreasing during processing) and a film that is an incompressible, Newtonian fluid (i.e., BMG supercooled liquid at elevated temperatures), the molding process can be modeled as a viscous thin film.

o  The small variation in pressure across the thickness of the film is neglected.

o  Although the flow is not at a steady state, inertial effects within the flowing film are neglected by a creeping flow assumption, which is supported by a low characteristic Reynolds Number of the flow.

o  The pressure at the edge of the mold is zero.

o  The area of the thin film is equal to the surface area of the mold.

o  The process is symmetric [8,10].

The molding process consists of three phases. First the film is heated to a constant temperature (e.g., 450°C) by contact with heated platens (see Fig. 2-1a.). It is then squeezed by a constant force applied equally by the upper platen and the nanopatterned molding chip (see Fig.2-1b.). Finally, once the molding process is completed, the film is rapidly quenched back to room temperature and the applied pressure is removed (see Fig. 2-1c.). The process produces a thin film of BMG between the mold and the platen.
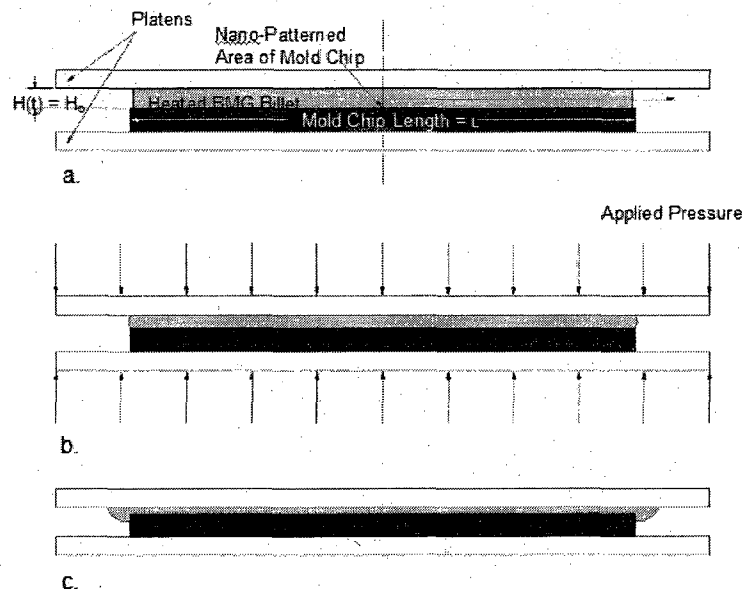


Figure 2-1: Macroscopic schematic of the molding process a) initially, b) as the BMG is squeezed and flows laterally, and c) with the final thin film of BMG between the mold and the platen [8,10].

To start the model, a simplification of the Navier-Stokes equations and the continuity condition for a squeezed viscous film yields:

$$\frac{1}{\mu}\frac{d}{dx}\left(H^3\frac{dp}{dx}\right)=-12\frac{dH}{dt}$$

(2-1)

where $\mu$ is the viscosity, $x$ is the lateral distance from the center of the mold, $H$ is the film thickness (see Fig. 2-1), t is the time, and $p$ is the local pressure within the thin film. This equation is commonly known as the Reynolds Equation for a squeezed film [16]. Taking advantage of symmetry, this expression is integrated from the center of the mold ($x=0$) to the edge of the squeezed film ($x=L/2$, where $L$ is the total width of the mold) to yield the lateral pressure gradient in the film of BMG:

$$\frac{dp}{dx}=-\frac{12\mu}{H^3}\frac{dH}{dt}x+C_1$$

(2-2)

where the constant of integration, $C_1$, is zero due to the symmetry boundary condition at the center of the chip.

$$\left.\frac{dp}{dx}\right|_{x=0}=0$$

(2-3)

Integrating a second time and applying the free surface condition at the edge of the chip

$$p(L/2)=0$$

(2-4)

the pressure distribution in the film is:

$$p_{BMG}(x,t)=-\frac{6\mu}{H(t)^3}\frac{dH}{dt}\left(x^2-\frac{L^2}{4}\right)$$

(2-5)

Note that the pressure is a function of time and location, and the film thickness is a function of time. In order to substitute for the film thickness function, the average applied pressure is equated with the undefined film pressure as depicted in Fig. 2-2.

10
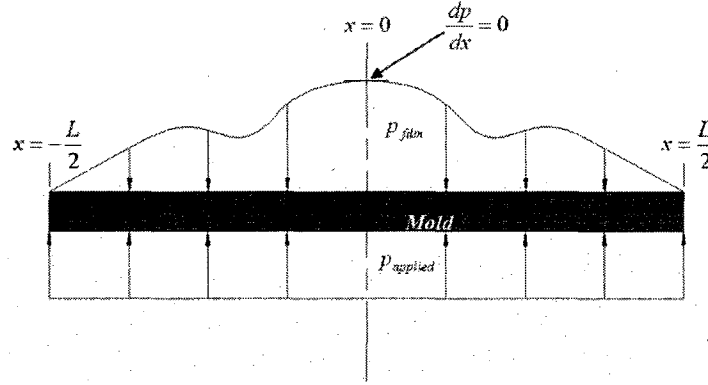
Figure 2-2: Schematic of molding process including definitions of parameters [8,10].

$$\int_0^{L/2} P_{applied}\,dx = \int_0^{L/2} P_{BMG}\,dx$$

(2-6)

The BMG film pressure is defined by Eq. 2-5, and the applied molding pressure is constant with respect to time and location on the surface of the mold chip:

$$P_{applied} = \frac{F}{A} = \frac{F}{L^2}$$

(2-7)

since the mold chip is square with a dimension of $L$. Substituting into Eq. 2-6:

$$\int_0^{L/2} \frac{F}{L^2}\,dx = \int_0^{L/2} \frac{6\mu}{H(t)^3}\frac{dH}{dt}\left(x^2 - \frac{L^2}{4}\right)dx$$

(2-8)

Performing these integrations and rearranging yields an expression for the thinning rate of the squeezed film, as a function of the film viscosity and known molding parameters:

$$\frac{dH}{dt} = -\frac{F}{L^4\mu}H^3$$

(2-9)

Note that the rate of film thinning *decreases* at a rate which is proportional to a reduction in film thickness cubed. From Eq. 2-5, the pressure within the film will *increase* at a rate which is proportional to a reduction in film thickness cubed. Therefore,

11

substitution of Eq. 2-9 into Eq. 2-5 results in a cancellation of the effect of the thinning film thickness. Subsequently, all time dependence of the pressure within the thin film of BMG is eliminated, since the film thickness was the only time dependent parameter in Eq. 2-5. Similarly, the effect of material viscosity also cancels out, yielding:

$$p(x)\big|_{film} = -\frac{3F}{2L^2}\left[\left(\frac{2x}{L}\right)^2 - 1\right]$$

(2-10)

Finally, substituting the applied molding pressure term (Eq. 2-7) into Eq. 2-10 yields:

$$p(x)\big|_{film} = -\frac{3}{2}p_{applied}\left[\left(\frac{2x}{L}\right)^2 - 1\right]$$

(2-11)

This expression allows for the determination of the local pressure within the squeezed film of BMG as a function of the known applied molding pressure. A properly scaled representation of the squeezed, thin film pressure distribution is provided in Fig. 2-3 [8,10]. This relationship will be used with an equation for the feature height based on the local pressure in the BMG to determine the feature height distribution over the mold chip.
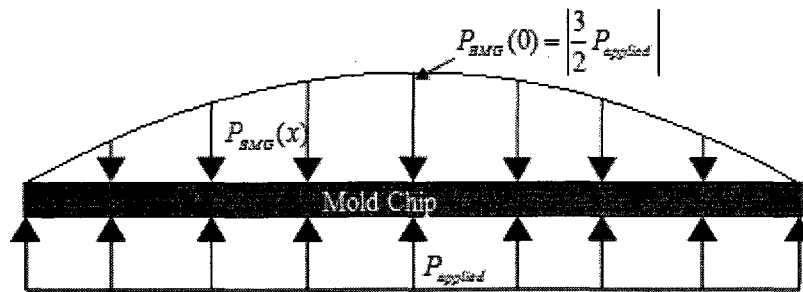


Figure 2-3: Predicted pressure distribution within the thin film of the BMG [8,10].

## 2.2 Nanoforming Model

In order to calculate the required pressure to cause viscous flow of the BMG into nanoscale features and the subsequent achievable feature height, a nano-molding theoretical model was developed based on a force equilibrium approach. A schematic of the flow of the BMG into the nanoscale mold features is shown in Fig. 2-4 [8,9]. The assumptions in this model are [8,9,11]:

o   Due to the nanoscopic size of mold features into which the BMG is flowing, the continuum assumption of fluid mechanics is validated by computation of the Knudsen number.

o   Inertial effects within the BMG are neglected. This is validated by calculating the Reynolds number.

o   The pressure induced by compressing the air in the mold features is neglected since by using the ideal gas law, it can be found that this pressure is much less than the typical molding pressures.

o   A frictionless condition is assumed for the flow, and therefore a pressure term to account for the frictional effect between the advancing flow and the mold feature is neglected.
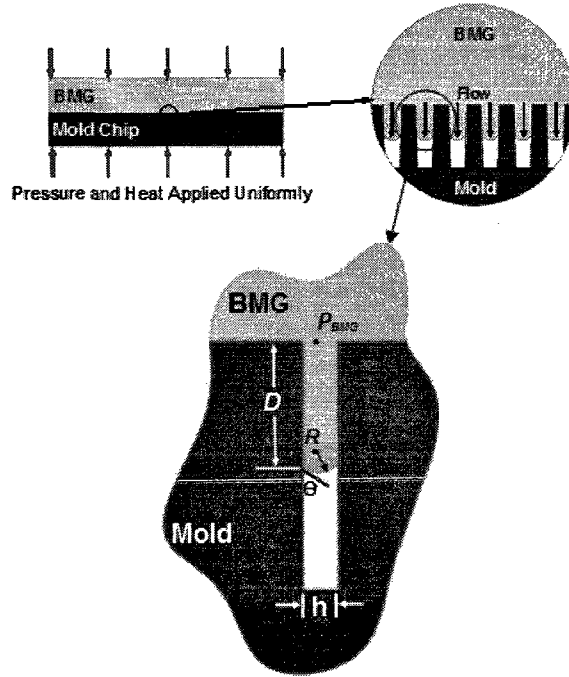
Figure 2-4: Schematic of molding process including definitions of parameters [8,9].

For molding to occur, the viscous ($\mu$) and capillary ($\gamma$) pressures must be overcome. These pressures can be modeled separately, $P_\mu$ and $P_\gamma$ respectively, and equated to the applied pressure to satisfy equilibrium [4,8,9,11]:

$$P_{BMG} = P_\mu + P_\gamma \tag{2-12}$$

The capillary pressure was assumed to be worst case, with complete anti-wetting between the BMG and the mold trench (i.e. $\theta$=0 in Fig. 2-4). This results in a semicircular meniscus of flow into the mold feature, with a radius, $R$, equal to one half of the mold trench width, $h$. An experiment was conducted, in which it was assumed that no viscous flow ($P_\mu$=0) occurred [8]. Eq. 2-12 may then be written as:

$$P_{BMG} = P_\gamma \tag{2-13}$$

14

The radius of curvature was found to be 182 nm. A value of surface tension was then calculated to be 27 N/m using Eq. 2-14 [8]. Ultimately, the capillary pressure was determined to be approximately 150 MPa [8].

$$\gamma = P_{BMG} R \tag{2-14}$$

Pressure loss due to viscous dissipation is modeled as a modified version of the pressure drop experienced by viscous Poiseuille flow. The modification is required to account for the depth of flow, $D$, varying with time, $t$, as the BMG fills the initially empty trench features [8,9,11].

$$P_\mu = \frac{12\mu}{h^2} D(t) \frac{dD(t)}{dt} \tag{2-15}$$

Solving this differential equation results in:

$$D(t) = h \sqrt{\frac{P_\mu}{6\mu} t} \tag{2-16}$$

The viscosity of the BMG is $\mu$ which is a function of temperature, see Fig. 1-8. Note that the instant $t = 0$ is defined as the onset of viscous flow, which cannot occur until the capillary pressure is overcome by the applied molding pressure [8,9,11]. Also note that the time is limited by the crystallization of the BMG.

## 2.3 Past Experimental Results

Silicon molds were initially produced using ion etching with PMMA as the photoresist to create trench features with an aspect ratio of approximately 1.4 as shown in Fig. 2-5a [8,9]. A molding experiment was conducted at 450°C for 2 minutes at 100Mpa using a Silicon die as shown in Fig. 2-5b. Feature heights, measured with an AFM to be

470nm in height, were uniform over the patterned area, and had an aspect ratio of approximately 1.3 [8,9]. Since the mold trench was almost completely filled, results were unable to validate the models. The effect of pressure distribution could not be observed most likely due to a small patterned area, and the aspect ratio was limited by the mold depth.
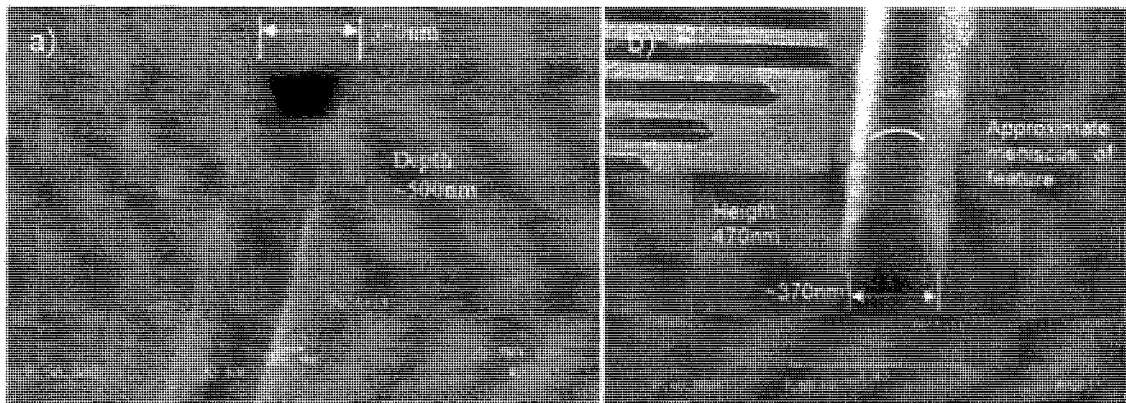


Figure 2-5: a) SEM image of Si mold b) SEM image of a Vit-1b specimen formed into a Silicon mold at 450°C at 100Mpa. Specimen's tilts are 80° providing a near cross sectional view of feature meniscus [8].

In order to validate the theoretical model, molds with a larger array of features needed to be investigated. Mold chips were designed taking this into consideration. The molds were designed to have varying sized trenches, triangular trenches and holes. The features were to be repeated over a 5mm x 5mm and 10mm x 10mm mold area. These molds were to be fabricated to contain high aspect ratio features. The process that was to be used was deep reactive ion etching (DRIE) with ZEP as the photoresist in order for the high aspect ratio to be obtained. The results of this investigation will be discussed in Chapter V, Section 3.

CHAPTER III

SURFACE TENSION

## 3.1 Background

In past research a nanomolding model was developed [8,11]. Assumptions within this model have led to quantitatively incorrect results, although qualitatively acceptable. One such assumption is the interface between the BMG and silicon is complete anti-wetting ($\theta = 0$). As can be observed from Figure 3-1, complete anti-wetting does not occur. A second assumption is that no viscous flow ($P_\mu = 0$) occurs while the features are being formed for the experiments conducted to find the capillary pressure.
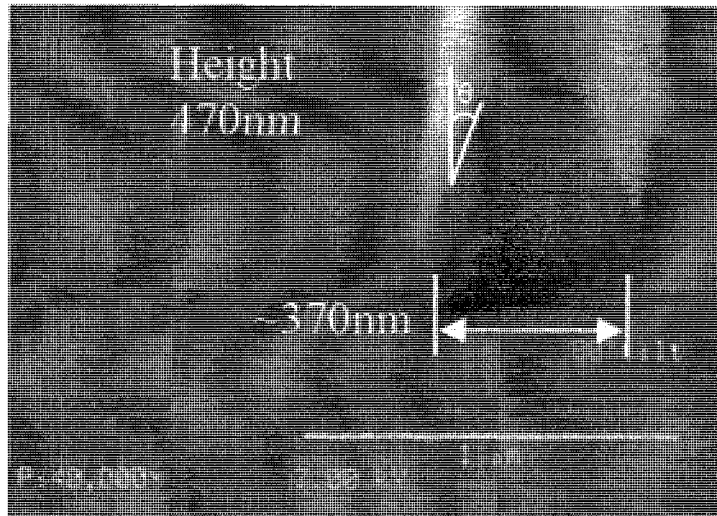


Figure 3-1: SEM image of a formed BMG feature from a silicon mold shows that complete anti-wetting ($\theta = 0$) does not occur [8].

Finding a more accurate surface tension value between the BMG and the silicon would eliminate these two assumptions that have partially led to the quantitative inaccuracies.

## 3.2 Determining surface tension

When the BMG is heated to a liquid, the surface tension between the BMG and Si is the surface tension between the liquid and solid, $\gamma_{SL}$. This can be modeled as puddle as shown in Fig. 3-2. The surface tension of the liquid BMG to air is that of the liquid to gas, $\gamma_{LG}$, and the surface tension of the silicon to air is that of the solid to gas, $\gamma_{SG}$. The angle between the liquid-gas surface tension and the solid-liquid surface is the contact angle, $\beta$. Note that the thickness and contact angle of puddles is relatively uniform and consistent for various size puddles of the same liquid on the same surface. This is shown in Fig. 3-3 for water on a waxed surface.
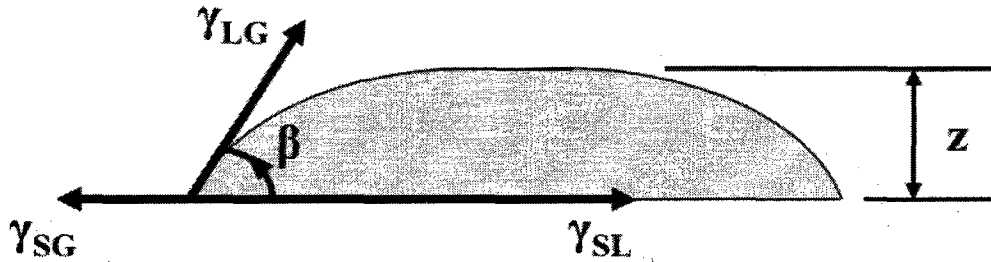


Fig. 3-2: Schematic of a puddle.
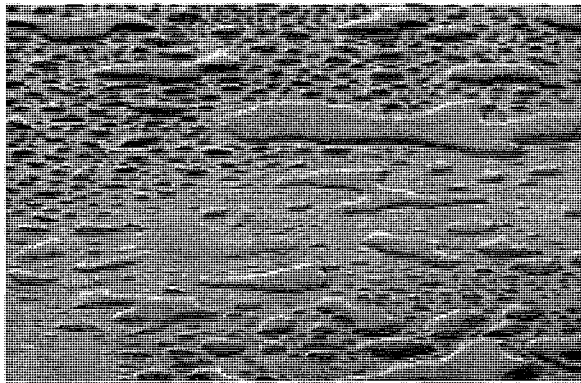


Figure 3-3: Water on a waxed surface shows that puddles have relatively consistent heights despite differences in the size of the puddles [12].

The height of the puddle, z, is given by [17]:

$$z = \sqrt{\frac{2\gamma_{LG}\left(1 - \cos(\beta)\right)}{\rho g}}$$

(3-1)

where β is the contact angle, shown in Fig. 3-2, ρ is the density of the liquid and g is the acceleration due to gravity. Rearranging Eq. 3-1 for the surface tension between the liquid and gas, $\gamma_{LG}$, yields:

$$\gamma_{LG} = \frac{\rho g \cdot z^2}{2\left(1 - \cos(\beta)\right)}$$

(3-2)

The surface tension of interest, between the liquid BMG and the silicon mold, can be described by the balance of forces of a liquid drop on a dry surface. This is entitled Young's equation and is given by [17]:

$$\gamma_{SL} = \gamma_{SG} - \gamma_{LG}\cos(\beta)$$

(3-3)

Young's equation assumes the surface is perfectly flat. Since silicon is a smooth material any surface roughness and impurities of the material that would cause inaccuracies in the result are negligible. Substituting in Eq. 3-2 into Eq. 3-3 yields:

$$\gamma_{SL} = \gamma_{SG} - \frac{\rho g \cdot z^2 \cos(\beta)}{2\left(1 - \cos(\beta)\right)}$$

(3-4)

The value of ρ for Vit-1b is 1.6 g/cm$^3$ [14]. In order to find the height of a puddle, z, and the contact angle, β, experiments were conducted. Silicon samples were heated in a heat treating oven to 1000+ K in order to melt the BMG. For Vit-1b the liquidus point is 1026 K [18]. The silicon samples were placed on a level surface near the edge of the door. Small volumes of BMG were then placed onto the heated silicon to allow a puddle to form. BMG was added after heating the oven and the silicon so that

crystallization would not occur. A digital camcorder was set to record time stamped pictures of the puddle from when the BMG is placed on the silicon until the BMG has been cooled. The camera was aligned such that with the oven door open the silicon front appeared as a 2D image. A schematic of the image seen by the camera is shown in Fig. 3-4. A Micro-Epsilon optris CT laser thermocouple with data recording, with a resolution of 0.1°C was used to record the temperature with respect to time.
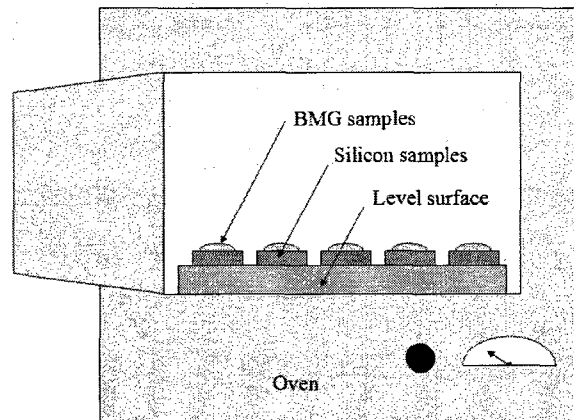


Figure 3-4: Schematic of oven with liquid BMG on silicon samples. Note that the sizes of BMG samples varied.

The experiments yielded no results as the BMG did not become liquid even with increased temperatures. BMG droplets have been formed before as shown in Fig. 3-5 [19]. The BMG not melting can most likely be explained by not conducting the experiments in a vacuum such as in Fig. 3-5. If oxidation occurred, the oxide layer may have prevented the melting process [20]. Experiments were not performed in a vacuum due to lack of time, cost, and lack of the facilities to conduct them in.
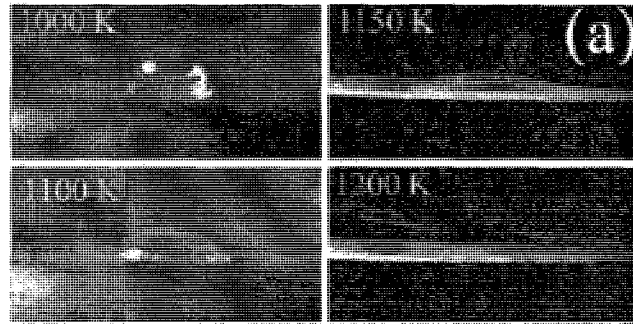
Figure 3-5: Images of Vit-1b processed on graphite discs at various temperatures [19].

The digital images were to be used to find z and $\beta$ values as a function of time. Note that scaling of the picture to find z values, could be performed by scaling to the known length of silicon samples. The time stamps of the temperature recordings would then be matched to the time stamps on the digital pictures to obtain values for z and $\beta$ as a function of temperature. As the temperature starts to cool, the contact angle will increase. As the contact angle increases, the puddle height will also increase. This concept is illustrated by Fig. 3-6.
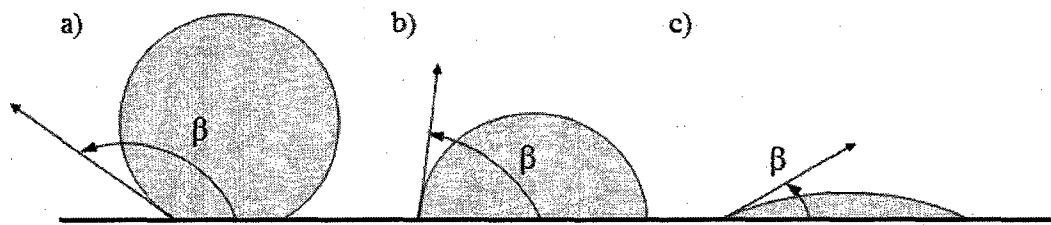


Figure 3-6: Illustration of the effect that higher contact angles produce a higher puddle height.

The z and $\beta$ results from the experiments substituted into Eq. 3-4 would produce a value for the surface tension of interest, $\gamma_{SL}$. Solving for $\gamma_{SL}$ at several temperatures

establishes a plot of $\gamma_{SL}$ as a function of temperature, so that these values can be used in the model. An example of this kind of plot for water is shown in Fig. 3-7.
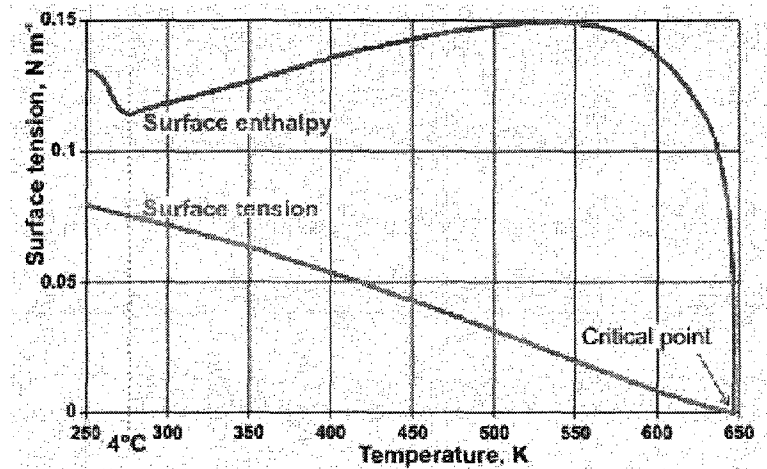


Figure 3-7: Plot of surface tension water, versus temperature [21].

Due to the inability to melt the BMG, the surface tension of the BMG on silicon is set to 1.47 N/m as suggested by Mukherjee et al. [15]. Although the surface tension of a material is known to vary with temperature this value is assumed to be constant for all temperatures. This is acceptable since temperature has a smaller effect on surface tension for metals than it does most liquids [22]. The surface tension for Vit-1 for higher temperatures than molding experiments is shown in Fig. 3-8 [15].
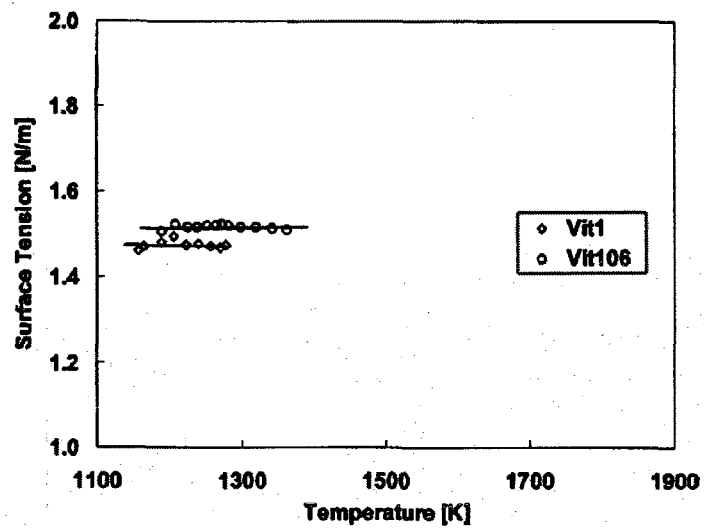
Figure 3-8: Surface tension for Vit-1 [15].

CHAPTER IV

THEORETICAL MODEL

## 4.1 Nanoforming Model

There are two modifications proposed to the model by Rason et al. [8,9]. The thin

film and nanoforming models discussed in Chapter II, section 1, and section 2,

respectively, were combined to form a single model with the modifications. First

capillary pressure is modeled through force equilibrium and the results to surface tension

discussed in Chapter III are applied.

Recall Eq. 2-12 [4,8,9,11]:

$$P_{BMG} = P_\mu + P_\gamma$$ (4-1)

where $P_\mu$ is the viscous pressure and $P_\gamma$ is the capillary pressure. The applied BMG

pressure here is the local pressure within the BMG, $P_{BMG}$, from Chapter II and is given

by:

$$P_{BMG} = -\frac{3}{2} P_{applied} \left[ \left( \frac{2x}{L} \right)^2 - 1 \right]$$ (4-2)

The length of the chip is $L$, the distance from center is $x$, and the applied pressure is

$P_{applied}$ [8].

When a liquid is unable to expand freely, there exists an interface with a second

liquid or gas. If this interface is curved, as in the case of the BMG to air interface while

BMG is being formed, there is a pressure difference across the interface. The capillary

pressure can be found by the force equilibrium depicted in Fig. 4-1b [23].
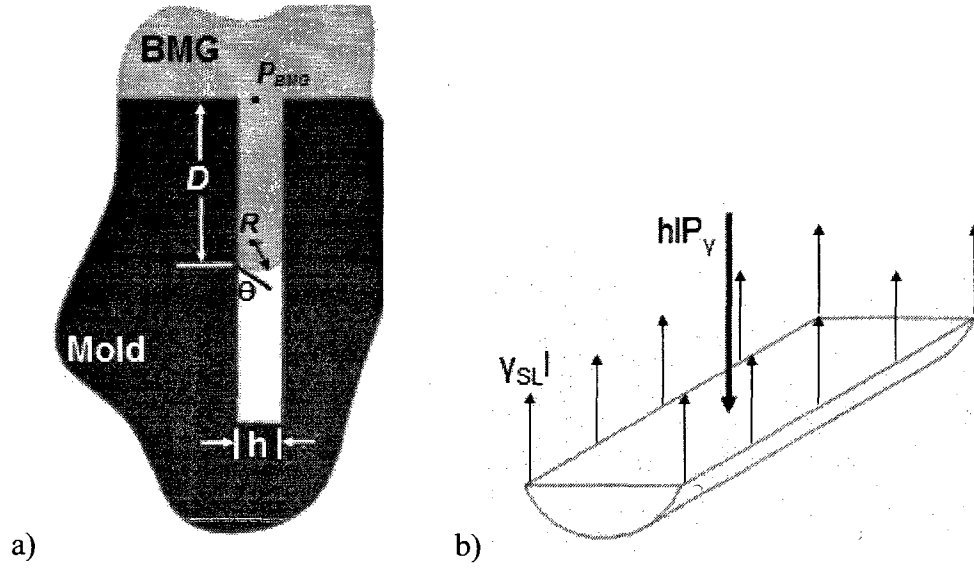
Figure 4-1: a) Schematic of molding process [8,9]. b) Pressure change across a curved interface due to surface tension [23].

From force equilibrium:

$$hlP_\gamma = 2 \cdot \gamma_{SL} l \tag{4-3}$$

The trench length, $l$, cancels out, so that $P_\gamma$ is a function of the trench width, $h$, shown in Fig. 4-1, and the surface tension of the liquid BMG on the Si mold. Rearranging for the capillary pressure:

$$P_\gamma = \frac{2\gamma_{SL}}{h} \tag{4-4}$$

Rearranging and substituting Eqs. 4-2 and 4-4 into Eq. 4-1 yields an expression for the viscous pressure:

$$P_\mu = P_{BMG} - P_\gamma = \frac{3}{2} P_{applied} \left[ \left( \frac{2x}{L} \right)^2 - 1 \right] - \frac{2\gamma_{SL}}{h} \tag{4-5}$$
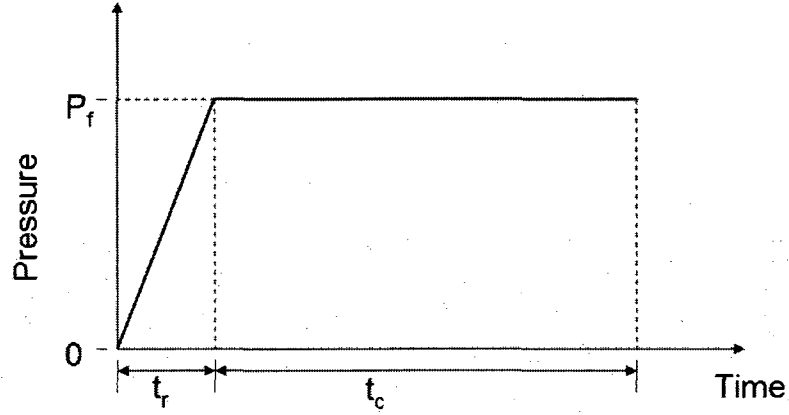
Figure 4-2: Pressure applied versus molding time.

Due to physical processing requirements to reach a constant applied pressure a ramp to the desired pressure is required (see Fig. 4-2). Thus flow occurs in two stages. Including both stages into the model is the second proposed change to the model by Rason et al. [8,9]. The first stage is during the ramp, and will be discussed later in this section. The second stage is while molding is at a constant applied pressure for a period of time, $t_c$. Note that time, $t$, is equal to the sum of $t_r$ and $t_c$. While $P_{applied}$ is constant, the viscous pressure, $P_\gamma$, is also constant so that the depth of flow is the only variable that is a function of time. Recall Eq. 2-15 [8,9,11]:

$$P_\mu = \frac{12\mu}{h^2} D(t) \frac{dD(t)}{dt} \qquad (4\text{-}6)$$

To obtain the depth of flow for which the pressure is constant, Eq. 4-6 is integrated and rearranged to yield:

$$D(t_c) = h\sqrt{t_c \cdot \frac{P_\mu}{6\mu}} \qquad (4\text{-}7)$$

Eq. 4-7 agrees with Rason et al. [8,9,11]. Substituting Eq. 4-5 into Eq. 4-7 yields:

$$D(t_c) = h\sqrt{t_c \cdot \frac{P_{BMG} - P_\gamma}{6\mu}} = h\sqrt{t_c \cdot \frac{\frac{3}{2}P_{applied}\left[\left(\frac{2x}{L}\right)^2 - 1\right] - \frac{2\gamma_{SL}}{h}}{6\mu}} \qquad (4\text{-}8)$$

The other molding stage in which filling occurs is during a ramp time, $t_r$, which is the time in which the pressure is being applied at a constant rate from zero to the final constant applied pressure. Recall that until the viscous pressure is overcome, the flow depth remains zero. However, from this point, which will occur along the ramp, to the constant applied pressure, flow occurs. To account for the depth of flow during the time of the ramp, $t_r$, Eq. 4-5 becomes:

$$P_\mu(t_r) = P_{BMG}(t_r) - P_\gamma = \frac{3}{2}P_{applied}(t_r)\left[\left(\frac{2x}{L}\right)^2 - 1\right] - \frac{2\gamma_{SL}}{h} \qquad (4\text{-}9)$$

The applied pressure, $P_{applied}(t_r)$ in Eq. 4-9 is a function of the ramp rate, $R_{rate}$, the area of the mold chip, $L^2$, and time it takes to get to pressure, $t_r$, and is given by:

$$P_{applied}(t_r) = \frac{R_{rate}t_r}{L^2} \qquad (4\text{-}10)$$

Note that $P_{applied}$ is a function of time here, while Eq. 4-5 is not. Now integrating Eq. 4-6 with the pressure varying with ramp time and rearranging for the depth of fill yields:

$$D(t_r) = h\sqrt{\frac{\frac{3}{2}\frac{R_{rate}}{L^2}\left[\left(\frac{2x}{L}\right)^2 - 1\right] \cdot \frac{1}{2}t_r^2 - \frac{2\gamma_{SL}}{h} \cdot t_r}{6\mu}} \qquad (4\text{-}11)$$

To find the total depth of fill, the results of Eqs 4-8 and 4-11 can be summed together to yield Eq. 4-12.

27

$$D(t) = h \sqrt{t_r \frac{\frac{3t_r}{2} \frac{R_{rate}}{L^2} \left[ \left( \frac{2x}{L} \right)^2 - 1 \right] - \frac{4\gamma_{SL}}{h}}{12\mu}} + h \sqrt{t_c \frac{3P_{applied} \left[ \left( \frac{2x}{L} \right)^2 - 1 \right] - \frac{4\gamma_{SL}}{h}}{12\mu}} \qquad (4\text{-}12)$$

Note that no fill will occur until $P_{applied}$ is greater than $P_\gamma$ to overcome the capillary pressure of Eq. 4-4. Also note that the molding temperature is a critical processing parameter even though not explicitly included in Eq. 4-12, since viscosity and surface tension are affected by the temperature.

## 4.2 Theoretical Results

Using Eq. 4-12 the depth of fill for various trench widths, h, with respect to the distances from the center of the mold can be predicted. A plot of the results is shown in Fig. 4-3. The processing parameters were a temperature of 450°C, a time of 65 sec, and a pressure of 100 MPa. The ramp rate was 0.08 kN/s and the viscosity was 30 MPa·s. As expected, as the trench width increases, the depth of fill increases, and as the distance from center increases, the depth of fill decreases.
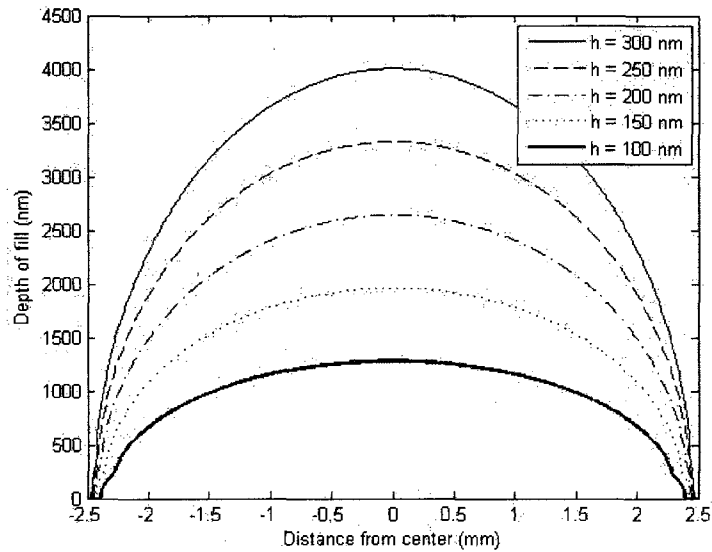
Figure 4-3: Plot of depth of fill vs. distance from center for various trench widths, with processing parameters: temperature (450°C), time (65 sec), and pressure (100 MPa).

The effects of the applied pressure on the depth of fill can be observed in Fig. 4-4. An increase in the applied pressure for a known time, temperature, and trench width, increases the depth of fill. Again the pressure distribution across the mold exists, where the greatest depth of fill occurs at the center. The plot shown in Fig. 4-4 can be normalized in order to show the achievable aspect ratio for different applied pressures and a known time and temperature (see Fig. 4-5).
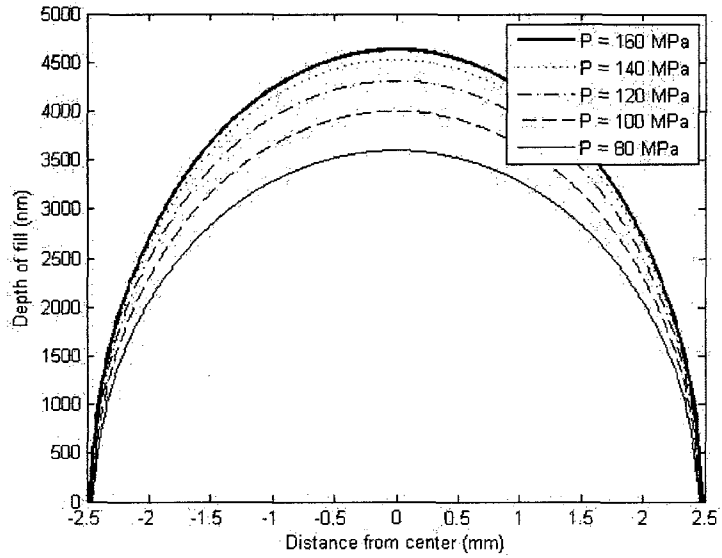
Figure 4-4: Plot of depth of fill vs. distance from center for various applied pressures, for a temperature of 450°C, a time of 65 sec, and trench width of 300 nm.
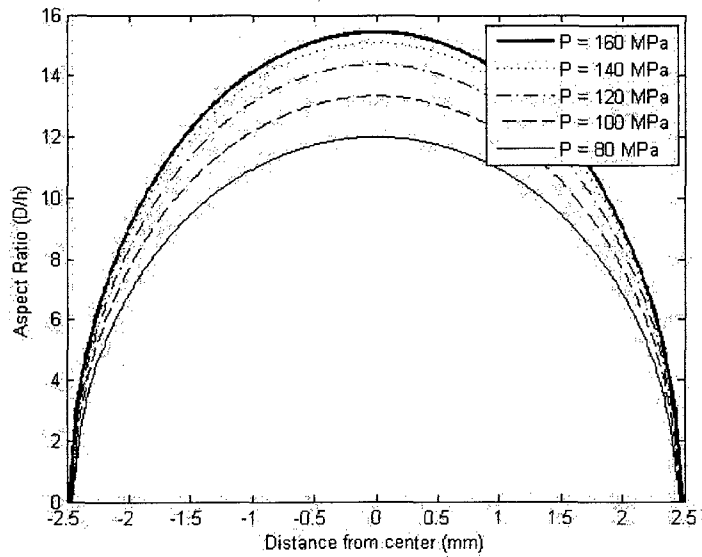


Figure 4-5: Plot of achievable aspect ratio vs. distance from center for various pressures for a temperature of 450°C, and a time of 65 sec.

Although temperature is not a variable in part of Eq. 4-12, viscosity is directly affected by temperature. Thus, the temperature will affect the depth of fill. As can be

seen from Fig. 4-6, as temperature increases the depth of fill increases. It should be noted that the crystallization time of the BMG decreases rapidly, allowing less time for the molding process to occur, and thus decreasing the distance between curves. Fig. 4-6 was created for 80% of the crystallization time of the BMG found in Fig. 1-8. The highest achievable aspect ratio for different temperatures and a known time and pressure is shown in Fig. 4-7. While it is obvious that increasing the temperature to 500°C will drastically increase the depth of fill, the crystallization time is approximately 30 seconds, not allowing for much processing time. Note that Fig. 4-7 was done for a processing time of 65 seconds, in which crystallization would occur for the 500 C case and flow would stop 30 seconds into the experiment.
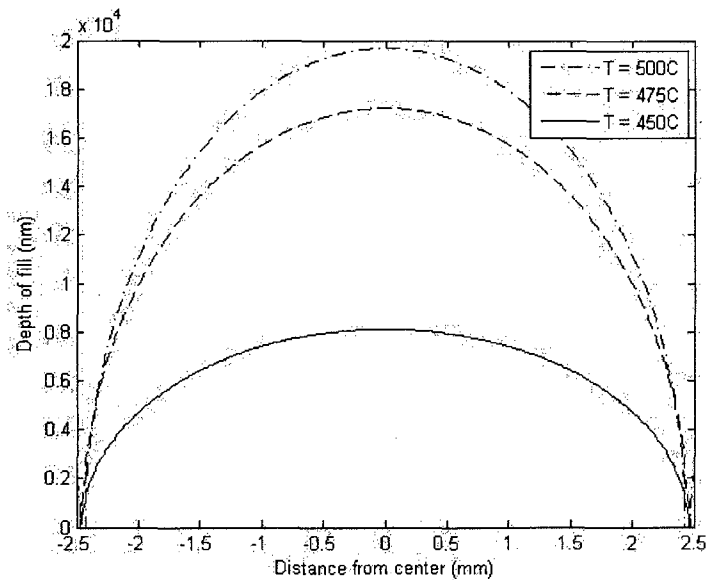


Figure 4-6: Plot of depth of fill vs. distance from center for various temperatures, a given pressure (100 MPa), time (80% of crystallization time) and trench width (300 nm).
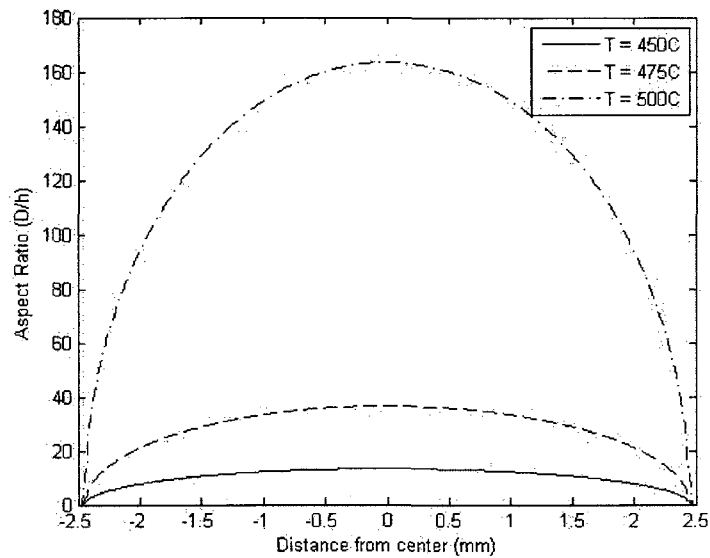
Figure 4-7: Plot of highest achievable aspect ratio vs. distance from center for various temperatures, a given pressure (100 MPa) and time (65 sec).

The results produced from Eq. 4-12 in Fig. 4-3 through 4-7 appear to be over predictions of the attainable depth of fills. The results may be too high due to the surface tension. A better prediction of surface tension would lead to a better prediction of the capillary pressure, resulting in a more reasonable depth of fill prediction. A large source of error that has led to an over prediction of fill is the BMG to silicon interface is not frictionless. Another source of error could be that other pressures ignored in the assumptions need to be taken into account, such as the backfilling pressure.

# CHAPTER V

## EXPERIMENTAL INVESTIGATION

### 5.1 Experimental Set-up

In order to test the validity of the theoretical model discussed in chapter IV, molds and an experimental set-up were designed. A custom fixture was installed on a model 1350 Instron mechanical testing machine which includes a pair of parallel H-13 tool steel platens (see Fig. 5-3, 5-4). Each of these platens is attached to another steel block that interfaces with the Instron (i.e. mounting blocks, see Fig. 5-3, 5-4). Cogetherm-P insulation blocks with ceramic standoffs are sandwiched between the platens and the mounting blocks in order to protect the rest of the set-up and Instron from heating. The bottom mounting block attaches directly to the Instron, while the top mounting block is attached to the bottom mounting block through a set of guide rods and springs with a spring constant of 0.01 kg/s$^2$. A steel ball sits on the top mounting block for a single point of contact with the Instron. This ensures the force applied by the Instron is perpendicular to the platens. The Instron is equipped with an Instron Corp. model number 3116-135 load cell with a capacity of 100 kN and a resolution of 0.05 N. A load is applied at a constant rate of 0.08 kN/s and then held at a constant load which is varied and controlled through a FastTrack8800LT control system to an accuracy of ±0.005% of the load cell capacity or 0.5% of the indicated load, whichever is greater. If the rate at which the load is applied is too large, the mold can break. The rate chosen was the fastest to get to the desired applied pressure without breaking the molds and was found through

experimentation. Heating cartridges and cooling lines are incorporated into the platens for the accurate heating and subsequent rapid quenching of molded specimens. The heating cartridges, manufactured by Omron are 6.35 mm diameter 50.8 mm long and produce a maximum temperature of approximately 550°C. The heating rate is shown in Fig. 5-1. Temperature is measured using K-type thermocouples with a resolution of 2.2°C and confirmed using a Micro-Epsilon optris CT IR sensor, with a resolution of 0.1°C. Note that due to data scatter at lower temperatures, the temperature at time zero is not ambient.
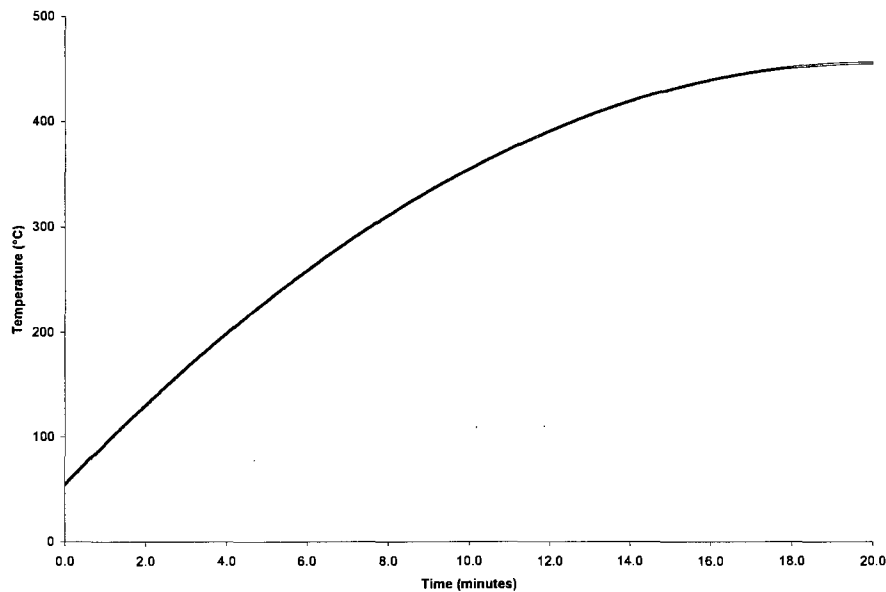


Figure 5-1: Plot of heating rate of experimental setup produced using K-type thermocouples with a resolution of 2.2°C.
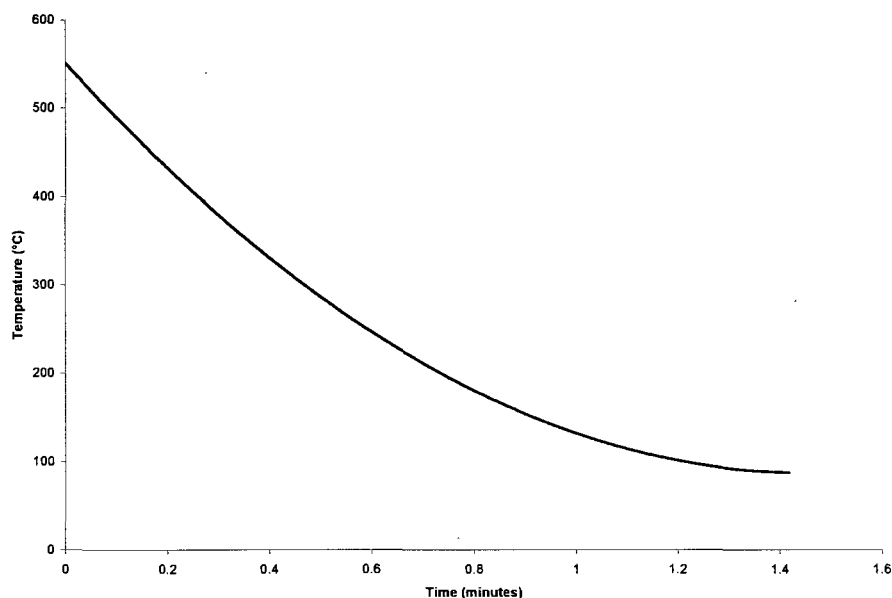
Figure 5-2: Plot of cooling rate of experimental setup produced using K-type thermocouples with a resolution of 2.2°C.

The cooling lines are attached to a circulating pump with an approximate flow rate of 530,000 $cm^3$/hr and provide a cooling rate depicted in Fig. 5-2. Note that between experiments the temperature was not necessarily reduced to ambient temperature in order to decrease the cycle time of the experiments. See Fig. 5-3 for a schematic of the system, and Fig. 5-4 for a picture of the experimental set-up.
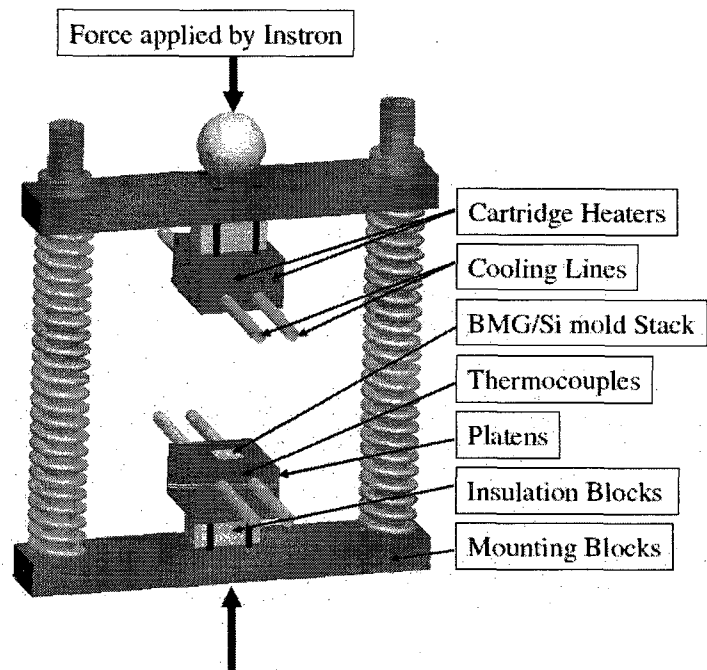
Figure 5-3: Schematic of experimental set-up including components for heating and cooling.
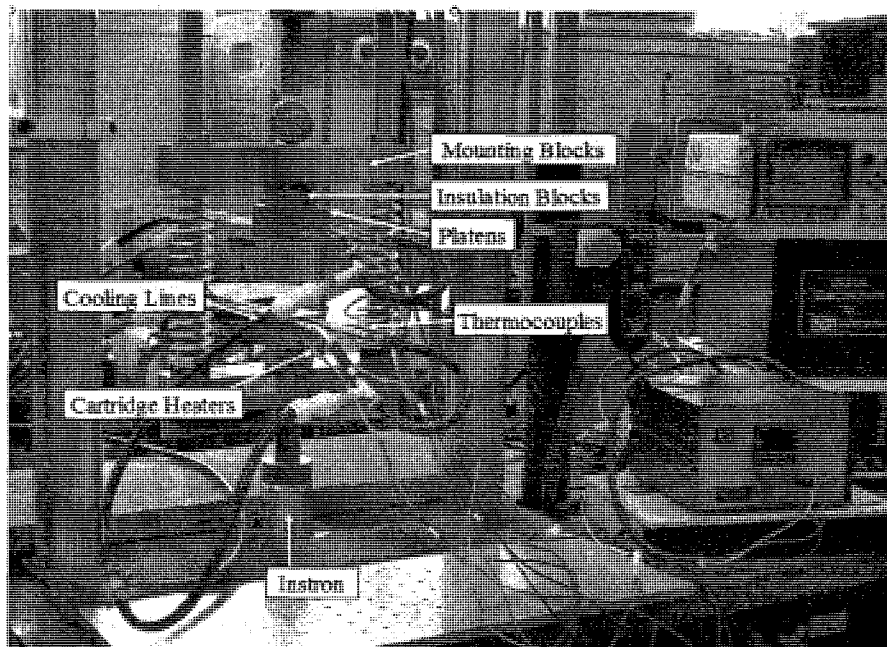


Figure 5-4: Picture of the experimental set-up.

A trade-off exists between the viscosity and the crystallization time as shown in Fig 1-8 for BMGs. Viscosity determines the flow characteristics of the BMG while the time is critical to assure that the BMG does not crystallize and the advantageous strength properties of the BMG remain. With a reduction of processing time through the quenching of the BMG, the process can be conducted at higher temperatures in order to decrease the viscosity, thus increasing the flow into the mold. The parameters used for molding experiments varied. The BMG is preheated before the pressure is applied, but is at temperature for no more than 75% of the crystallization time found from Fig. 1-8 except in the 500°C case. The BMG is rapidly quenched while pressure is still being applied to insure that the material does not flow back out of the nanoscale mold features.

## 5.2 Experimental Method

Experiments were conducted with the set-up described in the previous section and silicon molds to be discussed. Preparation for the experiment includes characterizing the mold with an SEM and AFM, and cleaning the BMG and silicon. The BMG is cleaned by soaking in alcohol, rubbing with a Q-tip while in the alcohol, and then blowing dry with compressed air. The silicon is first rinsed in acetone, followed by alcohol, and then soaked in a 110ºC heated piranha bath (i.e. 2:1 $H_2SO_4:H_2O_2$) for 10 minutes. It is then rinsed in deionized (DI) water before blowing dry to keep organic residue from forming.

The mold is then immediately placed on the platen to be preheated to temperature. Once temperature is reached as measured by the thermocouple, the BMG is placed onto the mold. The BMG is allowed to get to temperature, measured by the IR sensors before the pressure is ramped to a constant pressure based on the given test. While still under

pressure the BMG is rapidly quenched by the cooling lines in the platens. The BMG/silicon mold is then removed from the set-up.

In order to examine the BMG features, further processing must occur. When separating the BMG from the silicon, pieces of the silicon break and remain with the BMG. A 30% KOH bath is used to dissolve any remaining silicon on the BMG by soaking for 2 hours at 70°C-80°C. The BMG is then placed into an exothermic decontaminating bath (i.e. 5:1:1 $H_2O$:$H_2O_2$:$HCl$) for 20 minutes while still hot, rinsed in DI water, and then blown dry. The SEM and AFM are then used to measure the results.

## 5.3 Preliminary Experiments and Results

The molds briefly mentioned in Chapter II, Section 2 were fabricated and characterized. The silicon molds were produced to contain high aspect ratio (height/width) features in order to validate the theoretical model. Two sizes of mold chips were created via electron beam lithography and deep reactive ion etching with ZEP used as the resist. The first chip is 10mm x 10mm. These chips have 35 sets of features arranged as shown in Fig. 5-5a. Each set of features on the 10mm x 10mm chips consisted of 16 trenches, which were 400nm wide and approximately 800nm apart, a triangular trench, which was 3μm at its widest point, and 24 trenches, which were 200nm wide and approximately 1μm apart. All features were 110μm in length. These features are shown in the SEM image of Fig. 5-6 [10].
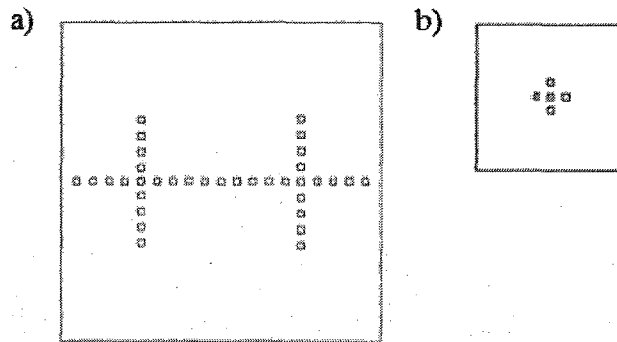
Figure 5-5: a) Arrangement of feature sets on the 10mm x 10mm chips and b) Arrangement of feature sets on the 5mm x 5mm chips [10].



Triangular Trench:
Length = 110μm
Width at top = 3μm

24 Trenches:
Width = 200nm
Length = 110μm
Spacing = 1μm

16 Trenches:
Length = 110μm
Width = 400nm
Spacing = 800nm
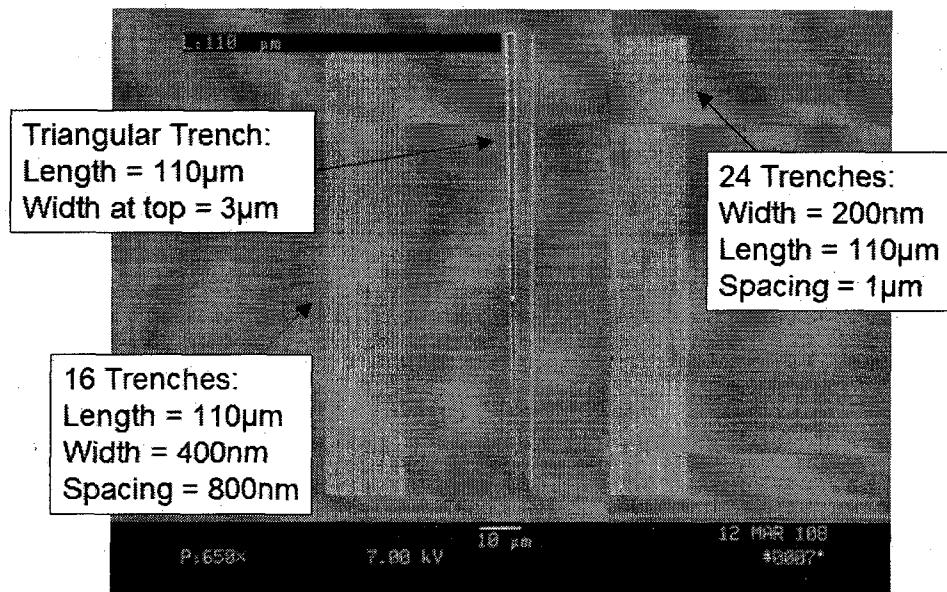
Figure 5-6: SEM image of 10mm x 10mm chip features [10].

The second chip is 5mm x 5mm. Each chip contains 5 sets of features arranged as shown in Fig. 5-5b with multiple sets of varied sized trenches and spacing. The arrangement of the feature types on the 5mm x 5mm mold is shown in Fig. 5-7. They also contain a triangular trench (see Fig. 5-8a) of the same measurements as the one on the 10mm x 10mm chips. Finally there is a set of holes as shown in Fig. 5-8b.

39

20 Trenches each:
Length = 60μm
Width decreases by 50nm
Spacing decreases by 150nm

Width = 300nm
Spacing = 900nm

Width = 50nm
Spacing = 150nm

20 Trenches each:
Length = 35μm
Widths = 300nm,
    200nm, 100nm
Spacings = 300nm,
    300nm, 100nm

Holes

Triangular Trench:
Length = 110μm
Width at top = 3μm
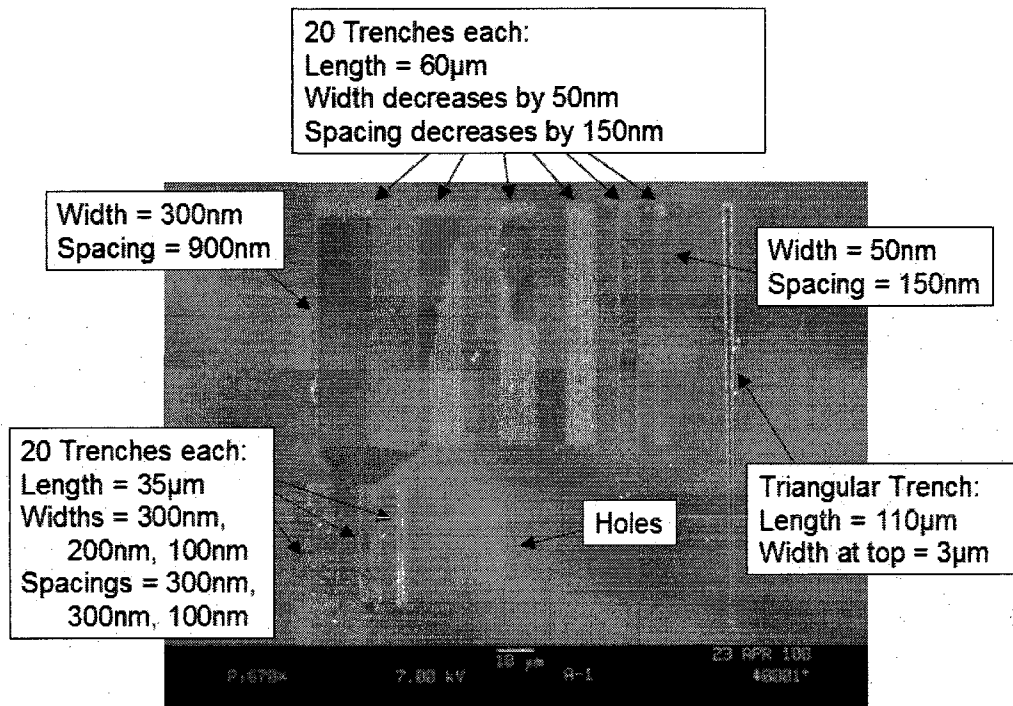
Figure 5-7: SEM image of 5mm x 5mm chip features [10].



a)

3μm wide x
2.5μm deep
at end

b)
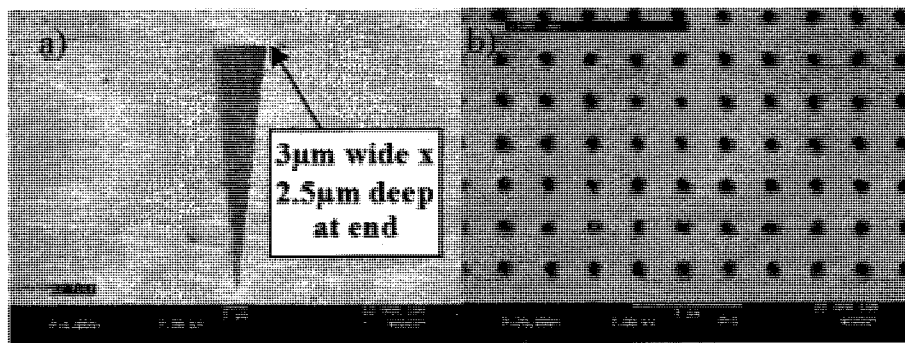
Figure 5-8: a) SEM image of triangular trench feature on both size chips and b) SEM

image of hole type features on 5mm x 5mm size chips [10].

40
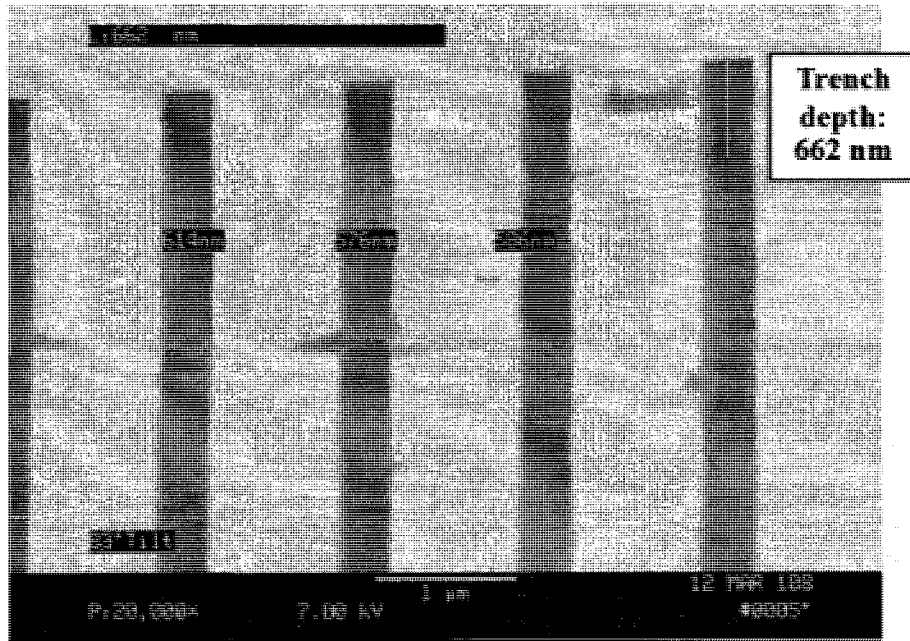
Figure 5-9: SEM image of sample set of trench features.

The depths on both sizes of chips vary from approximately 550nm to approximately 750nm. This creates aspect ratios ranging from 1.8 to 3 (see Fig. 5-9). The deep reactive ion etching did create higher aspect ratios than the molds in the past results shown in Chapter II, Section 2.

Experiments were conducted at 80MPa at 450°C. Flow into the trenches was limited (see Fig. 5-10), since capillary pressure was most likely not overcome. The bump features observed in Fig. 5-10 were limited. The holes in the molds did not show any indication of bumps on the BMG. The triangular trenches and the trenches showed the bump features. There was a trend in which the larger the feature size, the more pronounced the bump. Note that the diagonal marks in Fig. 5-10 are shear bands, which is how BMG is formed.
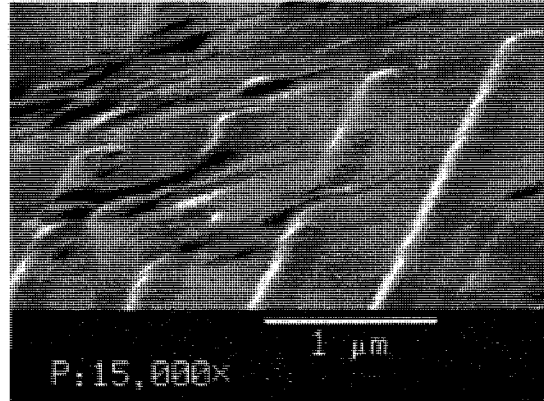
Figure 5-10: SEM image of BMG formed at 80MPa and 450°C.

Increasing the pressure to 100MPa at 450°C caused the silicon molds to shatter during the forming process. This may have been caused by the high feature density, 41 features per 0.0121mm² area for the lowest feature density chip, which created stress concentrations at each feature and resulted in broken molds. This phenomenon can be observed in the silicon molds, to be described in section 5.4, where cracks most likely due to stress were found near the features after molding experiments were conducted (see Fig. 5-11). The feature density may therefore be a limiting factor in producing features with this method.
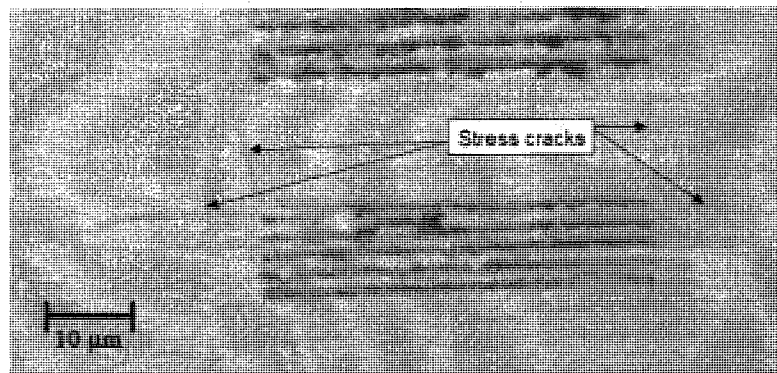


Figure 5-11: Microscope image of Si mold after molding experiment shows stress cracks around mold features.

## 5.4 Experiments and Results

An additional set of silicon molds were designed and fabricated to obtain high aspect ratio (height/width) features. These molds were specifically designed for validation of the theoretical predictions. In addition, the molds planned to have a lower density of features in order to reduce the breaking of molds. A single chip pattern was created by an external supplier, MEMS Exchange, who also created the molds discussed in the previous section, via electron beam lithography and deep reactive ion etching with ZEP used as the photoresist [24]. The size chip is 5mm x 5mm. Each chip is comprised of 11 patterned feature sets arranged as shown in Fig. 5-12. The varying distances from the center of the chip was designed to allow for validation of the thin film model.
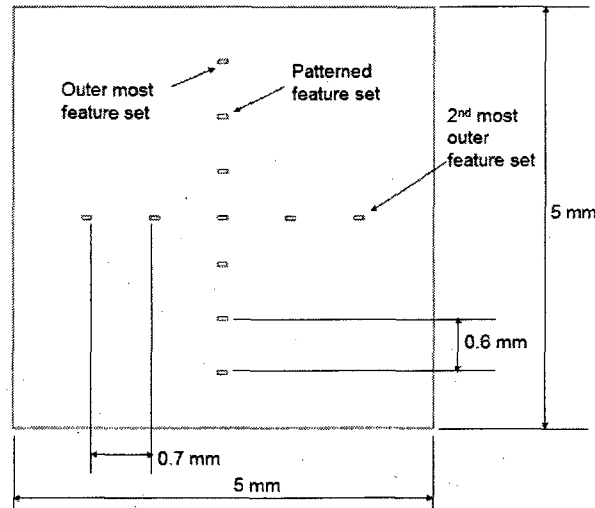


Figure 5-12: Arrangement of feature sets on a 5mm x 5mm chip.

These 11 patterned sets contain varying trench widths and feature spacings. Trenches were chosen for the feature of interest in order to compare with the 2D analytical model results. The widths of the trenches range from 300 nm to 100 nm in 50 nm increments, while the spacing between the trenches is 10 times the trench width.

These feature sizes were chosen to find the smallest feature sizes obtainable. Since 300nm trenches have been formed in the past, it was known that this trench width is formable [8]. Trench spacing was chosen in order to allow suitable feature densities to help prevent molds from breaking. The arrangement is shown in Fig. 5-13. An SEM image of this arrangement is shown in Fig. 5-14. Although the depths on these chips vary due to the feature sizes, the aspect ratio determined via SEM is approximately 5 for all feature sizes [24].
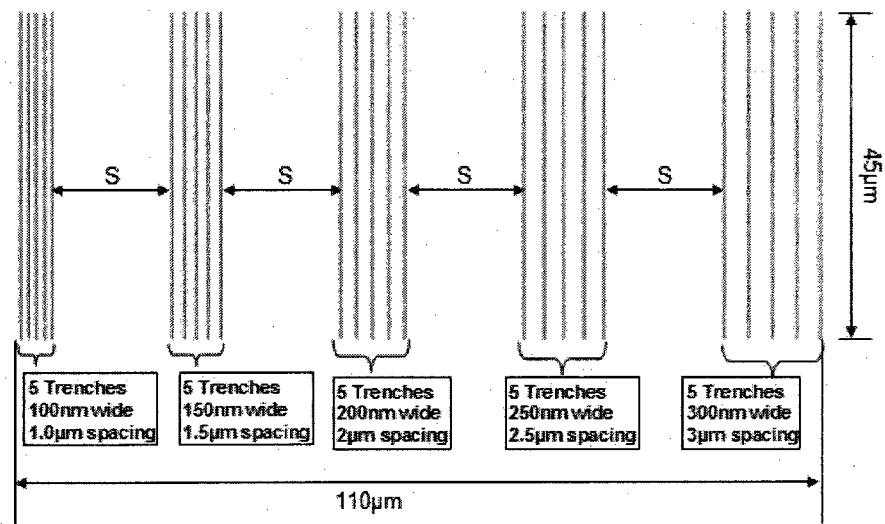


Figure 5-13: Trench sizes for each set of patterned features.
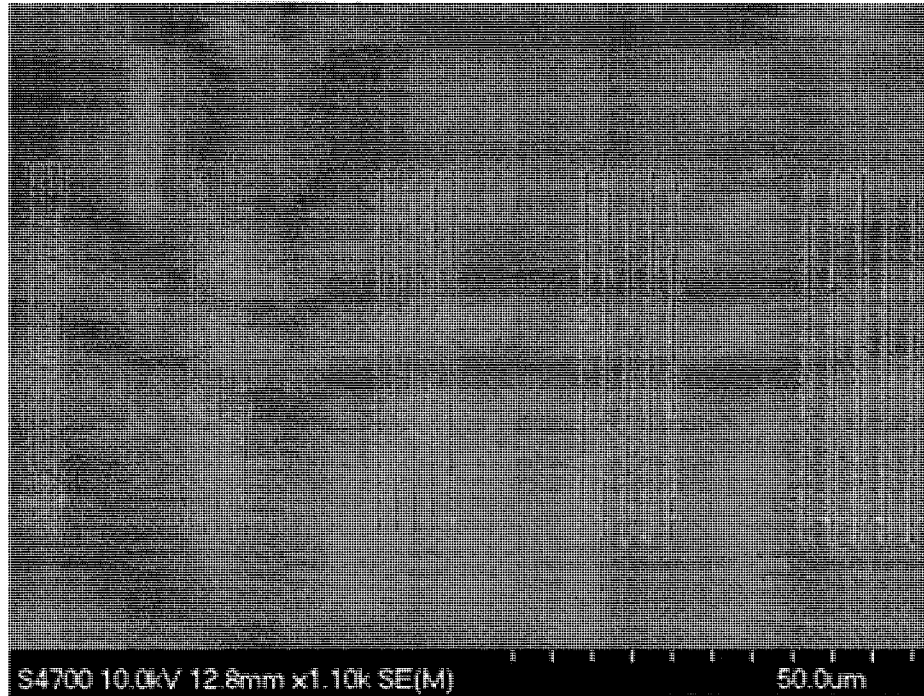
Figure 5-14: SEM image of a single patterned set [24].

Experiments were performed at varying temperatures, pressures, and times. These molding parameters are shown in Table 5-1. The viscosity value, $\mu$, was determined from Fig. 1-8 based on the molding temperature.

| Temperature (°C) | Viscosity (MPa·s) | Pressure (MPa) | Time (s) |
|---|---|---|---|
| 450 | 30 | 100 | 50 |
| | | | 65 |
| | | | 80 |
| | | 120 | 65 |
| | | 140 | 65 |
| 475 | 4 | 100 | 65 |
| | | 120 | |
| | | 140 | |
| | | 160 | |
| 500 | 0.2 | 100 | 50 |
| | | | 65 |

Table 5-1: Table of molding parameters used in experiments.

Again SEM images revealed that no fluid flow into the trenches was obtained, and thus molding was limited. An example of these molded features can be observed in Fig. 5-15. However, bump features on the molds confirmed the pressure was the highest at the center of the chip and decreased to the edges as evident by the number of features visible. An example of this array can be seen in Fig. 5-16. All samples were observed at a higher magnification (50 mag) than Fig. 5-16 (5 mag), and a sample set was verified using the SEM.
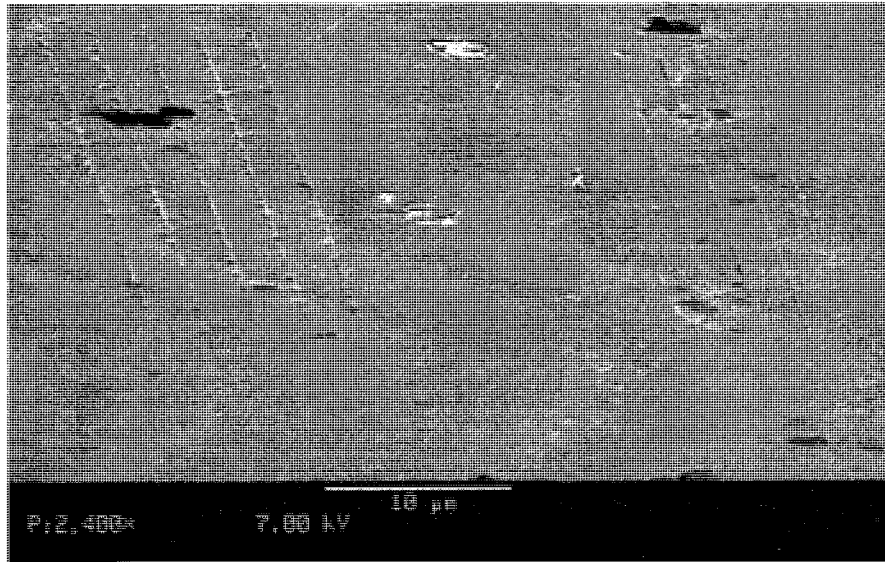


Figure 5-15: SEM image of two feature sets after a molding experiment.
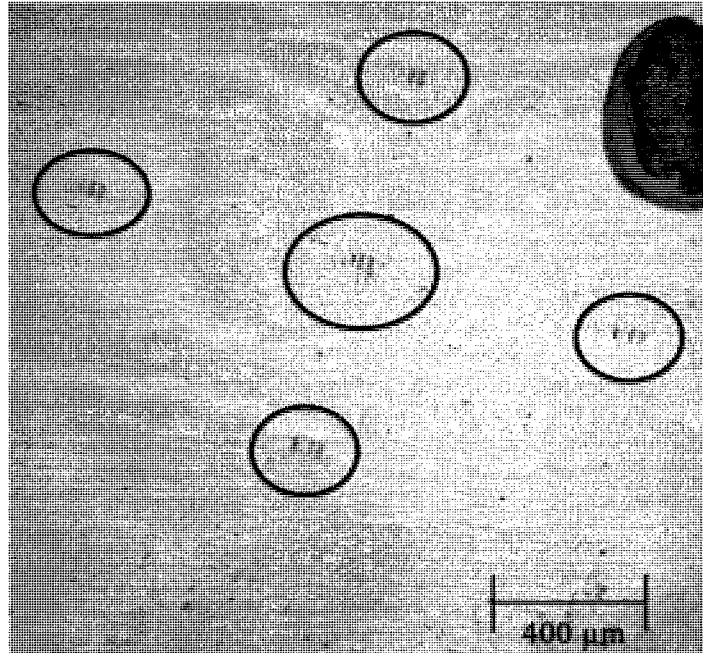
Figure 5-16: Microscope image of an example array of features and features sets in BMG.

The cause of the failed experiments is unknown. One possible explanation is that the particular alloy of BMG used, Vit-1b, may be affected by aging. The crystallization time has seemed to decrease and the melting temperature increased. When comparing experiments performed a year apart, with pieces from the same original sample, the time before crystallization had decreased significantly in the more recent experiments. This did not allow enough time for the flow of the BMG into the Si mold features.

Table 5-2 provides data for the effect of the applied molding pressure at a given temperature (475°C) and molding time (65 sec) on feature sets and feature sizes that can be observed. Pressure showed a predictable trend in both the feature sizes and the feature sets of the bumps achieved. With increasing pressure, more feature sizes were observed both in the center and outer feature sets. With respect to feature sets, there was

a slight increase in the number of feature sets observed with increasing pressure. This supports that a pressure distribution across the mold during the molding experiments does exist and affects the fill of the mold as the distance increases from the center. It should also be noted that the higher the pressure the more discoloration of the BMG was observed, which may indicate further crystallization or oxidation.

| Pressure (Mpa) | Feature Sets Observed | Feature Sizes Observed (Center) | Feature Sizes Observed (2nd outer most set) | Feature Sizes Observed (Outer most set) |
|---|---|---|---|---|
| 100 | All except outer most | 3/5 | 2/5 | 0/5 |
| 120 | All except outer most | 4/5 | 3/5 | 0/5 |
| 140 | All | 5/5 | 4/5 | 3/5 |
| 160 | All | 5/5 | 4/5 | 4/5 |

Table 5-2: Chart of the effect of applied molding pressure on the feature sets and feature sizes for a molding temperature of 475°C and a molding time of 65s.

When varying the molding time, there were slight differences observed with respect to bump features achieved (See Table 5-3). Fewer feature sets were produced with a shorter molding time. The same is true for the feature sizes observed at the outer most sets with fewer produced for a shorter molding time. For the case of 50 sec, 450°C, and 100 MPa molding parameters, the feature sizes observed decreased as distance from center increased. This indicates a pressure distribution as the distance from center increases.

| Time (s) | Feature Sets Observed | Feature Sizes Observed (Center) | Feature Sizes Observed (2nd outer most set) | Feature Sizes Observed (Outer most set) |
|---|---|---|---|---|
| 50 | All except outer most | 5/5 | 3/5 | 0/5 |
| 65 | All | 5/5 | 5/5 | 5/5 |
| 80 | All | 5/5 | 5/5 | 5/5 |

Table 5-3: Chart of the effect of molding time on the feature sets and feature sizes for a molding temperature of 450°C and a molding pressure of 100MPa.

The molding temperature had opposite trends than expected. Based on Fig. 1.8, increasing the temperature should decrease the viscosity and thus allow better flow of the material. Table 5-4 shows the effect of molding temperature on feature sets and feature sizes for three different molding pressures. For a given pressure, as temperature increases the number of feature sets and feature sizes (e.g., 140 MPa and 475 °C case) observed decreases. These observations contradict the expected effect of temperature due to decreases in viscosity and can be explained by crystallization occurring more rapidly than expected. Thus, care must be taken to prevent crystallization of the material.

| Pressure (Mpa) | Temperature (°C) | Feature Sets Observed | Feature Sizes Observed (Center) | Feature Sizes Observed (2nd outer most set) | Feature Sizes Observed (Outer most set) |
|---|---|---|---|---|---|
| 100 | 450 | All | 5/5 | 5/5 | 5/5 |
| | 475 | All except outer most | 3/5 | 2/5 | 0/5 |
| | 500 | None | n/a | n/a | n/a |
| 120 | 450 | All | 5/5 | 5/5 | 5/5 |
| | 475 | All except outer most | 4/5 | 3/5 | 0/5 |
| 140 | 450 | All | 5/5 | 5/5 | 5/5 |
| | 475 | All | 5/5 | 4/5 | 3/5 |

Table 5-4: Chart of the effect of molding temperature on the feature sets and feature sizes for various molding pressures and a molding time of 65s.

As temperature increased, it was observed that discoloration and brittleness, which was determined by how easily and into how many pieces the BMG broke when handled in similar manners, of the BMG increased. This is an indication of crystallization. X-ray diffraction tests verified that a crystalline structure was more prevalent in samples molded at higher temperatures (see Fig. 5-17). In Fig. 5-17 few peaks are observed in the 450 °C sample indicating a material that is mostly amorphous, while there are several more defined peaks in the 500 °C sample. Due to the brittleness of the 500 °C samples only a small piece of BMG could be analyzed in comparison to the

whole sample of the 450°C sample, causing a difference in the intensities recorded (i.e.,
y-axis of Fig. 5-17). Peak positions occur when the X-ray beam has been diffracted by
the lattice of the crystal. Since crystals are a periodic structure, the peaks should be
periodic when crystals are present. Thus the number of peaks observed in the 500C
sample shows the sample has been crystallized. The exact time in which crystallization
began to occur in experiments could not be determined. It is however, not surprising that
the 500°C case crystallized since heat was applied during the molding experiment for 65
seconds. Based on the TTT diagram (Fig. 1-7), crystallization occurs for this material
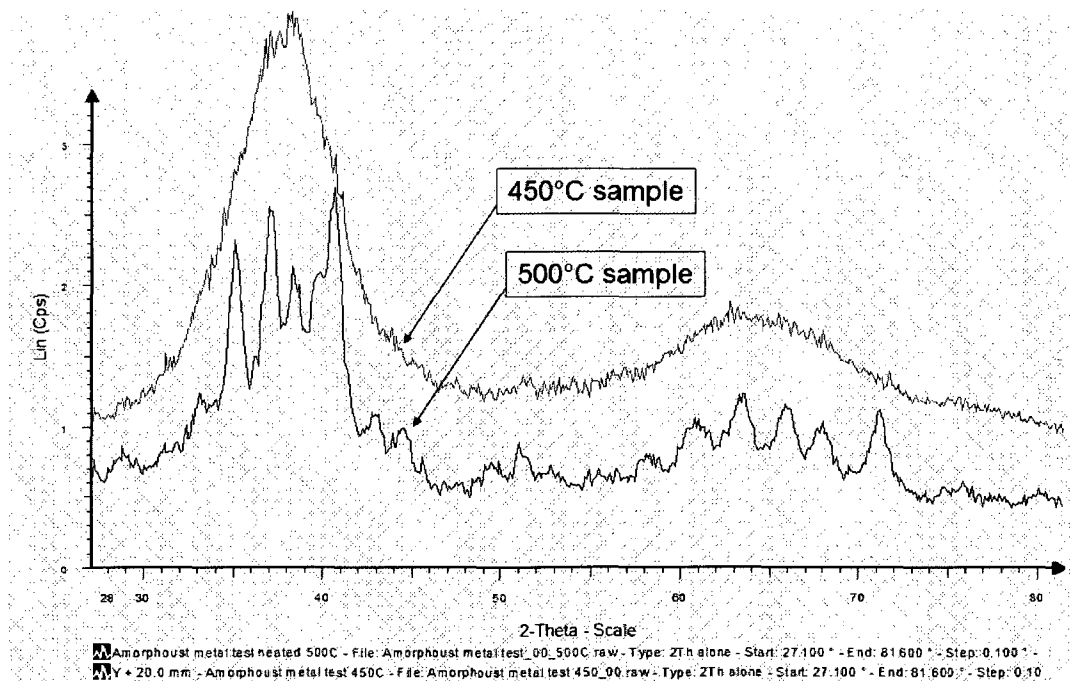when heated for approximately 30 seconds at 500°C.



Figure 5-17: X-ray diffraction plot of intensity (counts per sec) versus x-ray diffraction
angle. Plot shows BMG formed at a higher temperature crystallized, while lower
temperature remained mostly amorphous.

CHAPTER VI

CONCLUSIONS & FUTURE WORK

## 6.1 Conclusions

Nanosized features have been manufactured using the nanoforming process in the past. The goal is to create a cost effective mass production nanomanufacturing process to produce nanoscale parts.

In this research, a theoretical model for predicting the depth of fill as a function of mold location for a known set of molding parameters was further developed. The two past models were combined, and two modifications were proposed. The capillary pressure was modeled using force equilibrium. Also, since experiments apply the pressure at a constant ramp until the full pressure is reached, some filling will occur prior to the constant applied pressure. The depth of fill that occurs during the ramp was added to the depth of fill while being held at pressure, to find a total depth of fill. Also as part of the model development, the effect of surface tension for BMG on Si was considered.

Through experimentation it was found that the area density of features on a mold may create increased stress concentrations causing molds to break. A robust nanoforming process was implemented and low feature density molds were designed and fabricated in order to reduce the breaking of molds. The molds were produced using deep reactive ion etching to obtain high aspect ratio features.

Although complications in the experiments led to limited results, observations were made on the molding parameters (time, temperature, and applied pressure). With increased applied pressure, the number of features and feature sets visible increased.

Also, as the distance from center increased the quantity of features visible decreased for a given experiment. Although not as apparent as the pressure results, increased molding time also increased the number of features visible. These findings indicate that a pressure distribution across the mold exists. Temperature exhibited the opposite trend than expected; increased temperature decreased the number of features visible. This difference might be explained by crystallization, since temperature also affects the crystallization time. At higher temperatures further discoloration and brittleness of the BMG was observed.

## 6.2 Future Work

Due to the inability to create flow of the BMG into the features, quantitative results could not be found. In order to better compare experimental results and theoretical results, further research should be done in this area. It is important to properly predict the required parameters for filling the desired feature sizes in order to insure a low-cost, quality, high rate nanomanufacturing process. Two areas of experimentation should be completed in order to fully understand nanoforming.

The first area of experimentation that should be conducted is further investigations with the deep reactive ion etched molds discussed in Chapter V, Section 4. Experiments can be performed with a different alloy of BMG, or the same alloy newly manufactured. This would eliminate the possibility that the BMG degrades with age. These experiments can be used to find the highest achievable aspect ratio and the pressure distribution across the mold. The second area of experimentation needing to be explored further is the surface tension of BMG being used. Conducting the surface

tension experiments in a vacuum should allow the BMG to melt. This will result in surface tension values for the temperature range of molding experiments. These values can then be used to better predict the depth of fill in the theoretical model. The improvements in these two areas of experimentation should help make the theoretical predictions align quantitatively with the experimental results. While the pressure distribution across the mold has been observed qualitatively, the effects of pressure should be confirmed quantitatively by comparing experimental and theoretical results.

Ultimately the molds and/or molding process should be modified to allow for reusable molds. The silicon molds are brittle and can be used only once, since the material tends to break during molding process. This may be due to any non vertical forces, such as flow into features and forces due to possible slightly unparallel platens. A different material that is stronger in the lateral direction and more durable than silicon should be investigated, perhaps quartz. Note that a stronger mold material may also allow for a higher feature density. Also note that the wetability of the mold is important for ease of flow into features.

# LIST OF REFERENCES

[1] Sachin, B. "Thin Film Deposition on Plastic Substrates using Silicon Nanoparticles and Laser Nanoforming", *Journal of Materials Science and Engineering* B, 2006, pp. 228-236.

[2] Saotome, Y., Itoh, K., Zhang, T. and Inoue, A. "Superplastic Nanoforming of Pd-Based Amorphous Alloy," *Scripta Materialia*. 44, 2001, pp. 1541–1545.

[3] Saotome, Y., Hatori, T., Itoh, K., Zhang, T. and Inoue, A. "Superplastic micro/nano-formability of $La_{60}Al_{20}Ni_{10}Co_5Cu_5$ amorphous alloy in supercooled liquid state," *Materials Science & Engineering*. A304-306, 2001, pp. 716–720.

[4] Schroers, J. "The Superplastic Forming of Bulk Metallic Glasses", *Journal of Metals*, May 2005, pp. 35-39.

[5] Kumar, G., Tang, H., Schroers, J. "Nanomoulding with amorphous metals", *Nature Letters*, Dec. 2008, pp. 1-5.

[6] LiquidMetal Technologies, Inc., www.liquidmetal.com

[7] Bardt, J.A., Ziegert, J.C., Schmitz, T., Sawyer, W.G., and Bourne, G., "Micromolding Three-Dimensional Amorphous Metal Structures", *Journal of Materials Research*, Vol. 22, No. 2, 2007, pp. 339-343.

[8] Rason, K. "Nanoscale Molding of Bulk Metallic Glass", University of New Hampshire, M.S. Thesis, September 2007.

[9] Rason, K., Kinsey B. "Nanoscale Molding of a Zirconium Based Bulk Metallic Glass", ASME International Mechanical Engineering Conference and Exposition, Seattle, WA, Nov. 2007.

[10] Mros, C., Kinsey B., Rason, K. "Validation of Superplastic Forming Models for Nanoscale Bulk Metallic Glass Features", *ASME International Mechanical Engineering Conference and Exposition*, Boston, MA, Oct. 31-Nov. 6 2008.

[11] Mros, C., Kinsey B., Rason, K. "Nanoscale Molding Model for Nanoscale Bulk Metallic Glass Features", *ASME International Manufacturing Science and Engineering Conference*, West Lafayette, IN, Oct. 4-7 2009.

[12] Google Images, www.google.com

[13] Vollertsen, F., Hu, Z., Niehoff, H.,S., Theiler, C, "State of the art in micro forming and investigations in micro deep drawing", Journal of Materials Processing Technology, Vol. 151, No. 1-3, 2004, pp. 70-79.

[14] Schroers, J., Pham, Q., Desai, A., "Thermoplastic Forming of Bulk Metallic Glass-A Technology for MEMS and Microstructure Fabrication", *Journal of Microelectromechanical Systems*, v16 N 2, April 2007 pp. 240-7.

[15] Mukherjee, Johnson W., and Rhim, W. "Non-contact Measurement of High-Temperature Surface Tension and Viscosity of Bulk Metallic Glass-Forming Alloys Using the Drop Oscillation Technique", Applied Physics Letters 2005 86, 014104.

[16] R. Panton, Incompressible Flow, Wiley-Interscience 1984.

[17] Gennes, Pierre-Gilles De. Capillarity and wetting phenomena drops, bubbles, pearls, waves. New York: Springer, 2003.

[18] Masuhr, A., Busch, R., and Johnson, W.L. Material Science Forum 269-272,779 (1998).

[19] Schroers, J., Samwer, K., Szuecs, F. and Johnson, W.L. "Characterization of the interface between the bulk glass foming alloy $Zr_{41}Ti_{14}Cu_{12}Ni_{10}Be_{23}$ with pure metals and ceramics", *Materials Research Society*, Vol. 15, No. 7, July 2000, pp. 1617-1621.

[20] Schroers, J. "Re: possible collaboration on nanomolding BMG project." Email to B. Kinsey. 23 Oct. 2009.

[21] Chaplin, M. "Explanation of the Physical Anomalies of Water." London South Bank University, UK. 11 Aug. 2009 <http://www1.lsbu.ac.uk/water/explan5.html>.

[22] Iida, T., Guthrie, R., "The Physical Properties of Liquid Metals", Oxford Science Publications, Clarendon Press, Oxford, 1987.

[23] White, F. M. *Fluid Mechanics*. New York: McGraw-Hill Companies, 2002.

[24] Mems Exchange Inc., www.Mems-exchange.org